OPTIMIZATION OF NICKEL SEED LAYER FOR PERC PLATING METALLIZATION

A THESIS SUBMITTED TO
THE GRADUATE SCHOOL OF NATURAL AND APPLIED SCIENCES
OF
MIDDLE EAST TECHNICAL UNIVERSITY

BY

MELISA KORKMAZ ARSLAN

IN PARTIAL FULFILLMENT OF THE REQUIREMENTS
FOR
THE DEGREE OF MASTER OF SCIENCE
IN
MICRO AND NANOTECHNOLOGY

SEPTEMBER 2023

Approval of the thesis:

OPTIMIZATION OF NICKEL SEED LAYER FOR PERC PLATING METALLIZATION

submitted by **MELISA KORKMAZ ARSLAN** in partial fulfillment of the requirements for the degree of **Master of Science** i**n Micro and Nanotechnology, Middle East Technical University** by,

Prof. Dr. Halil Kalıpçılar
Dean, **Graduate School of Natural and Applied Sciences**

Prof. Dr. Deniz Üner
Head of the Department, **Chemistry**

Prof. Dr. Raşit Turan
Supervisor, **Physics, METU**

Assoc. Prof. Dr. Hüsnü Emrah Ünalan
Co-Supervisor, **Metallurgical and Materials Eng, METU**

Examining Committee Members:

Prof. Dr. Mehmet Parlak
Physics, METU

Prof. Dr. Raşit Turan
Physics, METU

Prof. Dr. Alpan Bek
Physics, METU

Assoc. Dr. Mustafa Kulakcı
Physics, Eskisehir Technical Uni.

Assist. Dr. Veysel Ünsür
Department of Basic Sciences, Necmettin Erbakan Uni.

Date: 05.09.2023

I hereby declare that all information in this document has been obtained and presented in accordance with academic rules and ethical conduct. I also declare that, as required by these rules and conduct, I have fully cited and referenced all material and results that are not original to this work.

Name Last name : Melisa Korkmaz Arslan

Signature :

ABSTRACT

OPTIMIZATION OF NICKEL SEED LAYER FOR PERC PLATING METALLIZATION

Korkmaz Arslan, Melisa
Master of Science, Micro and Nanotechnology
Supervisor: Prof. Dr. Raşit Turan
Co-Supervisor: Assoc. Prof. Dr. H. Emrah Unalan

September 2023, 92 pages

One of the significant contributors to the costs of solar cell fabrication lies in the metallization process. Escalating prices of silver for front-side metal contacts have presented challenges to cost-effective production. To address this, alternative, cost-efficient metal contacts with compatible performance have gained momentum. This study proposes Ni/Cu/Ag plated metal contacts as a viable alternative for front-side metalization of solar cells. Incorporating a Ni seed layer is pivotal as a barrier, effectively eliminating the diffusion of Cu. A paramount objective is establishing a uniform and effective Ni seed layer regarding low contact resistivity. Sequentially, Ni seed layer formation is followed by the deposition of a Cu conductive layer and an Ag capping layer. These strategic steps collectively aim to provide a front metal contact for industrially feasible Passivated Emitter Rear Cell (PERC) cell production. The resultant samples exhibit a low contact resistivity comparable to the standard screen-printed Ag metallization approach. Consequently, with optimized Ni seed layer deposition and annealing parameters, contact resistance of approximately 8 mΩ/cm is achieved for Ni/Cu/Ag plated PERC solar cells, accompanied by an efficiency level of >16% by pilot scale industrial production approach.

Keywords: plated Ni/Cu/Ag, bias-assisted/light-induced plating, laser ablation, PERC, Ni seed layer

ÖZ

PERC TİPİ HÜCRELERİN KAPLAMA YÖNTEMİYLE NİKEL TOHUM KATMANININ OPTİMİZASYONU

Korkmaz Arslan, Melisa
Yüksek Lisans, Mikro ve Nanoteknoloji
Tez Yöneticisi: Prof. Dr. Raşit Turan
Ortak Tez Yöneticisi: Doç. Dr. H. Emrah Ünalan

Eylül 2023, 92 sayfa

Güneş hücresi üretim maliyetlerine önemli katkı sağlayan faktörlerden biri, metalizasyon işlemidir. Ön yüz metal kontakları için gerekli olan gümüşün artan fiyatı, düşük maliyetli üretimi zorlaştırmaktadır. Buna çözüm bulmak amacıyla, kıyaslanabilinir performans gösteren alternatif ve düşük maliyetli metal kontak için arayış hız kazanmıştır. Bu çalışma, güneş hücrelerinin ön yüz metal kontakları için umut vaat eden bir alternatif olarak Ni/Cu/Ag metal kontaklarını elektrokimyasal kaplama yöntemiyle oluşturulmasını önermektedir. Burada, nikel çekirdek tabakanın entegrasyonu, bakırın difüzyonunu etkili bir şekilde engellemek için bariyer olarak önemli bir rol üstlenmektedir. Temel amaç, düşük kontak direnci sağlayan, homojen ve etkili bir nikel çekirdek katmanının oluşturulmasıdır. Nikel çekirdek tabakasının üzerine sırasıyla, bakır iletken tabakası ve ince bir gümüş tabaka oluşturulmaktadır. Bu stratejik adımlar, pasifleştirilmiş emitör ve arka kontak (PERC) güneş hücrelerinin endüstriyel olarak uygun üretimi için ön metal kontak oluşumunu sağlamayı amaçlamaktadır. Bu yaklaşımla üretilen örnekler, standart ekran baskılı gümüş metalizasyon yaklaşımıyla kıyaslanabilecek düşük kontak direncine sahiptir. Sonuç olarak, optimize edilmiş nikel çekirdek tabakasının oluşturulması ve ısıl işlem parametrelerinin uygulanması sayesinde, Ni/Cu/Ag kontaklar için PERC güneş hücrelerinde yaklaşık 8 mΩ/cm temas direnci elde edilmiş ve %16'dan yüksek verimlilik seviyesine sahip hücreler pilot ölçekte endüstriyel yaklaşımla üretilmiştir.

Anahtar Kelimeler: Ni/Cu/Ag elektro kimyasal kaplama, nikel çekirdek katmanı, laser ile kaldırma, pasifleştirilmiş yayıcı arka kontak hücreleri (PERC)

To *my unwavering supporters throughout this journey, and to my ever-supportive family,*

ACKNOWLEDGMENTS

I would like to express my sincere gratitude to my advisor, Prof. Dr. Raşit Turan, for his exceptional support, and guidance, and for introducing me to the excellent SiPV group. His trust in me, along with his invaluable assistance in providing the necessary resources during my research, has been instrumental in shaping this thesis.

I extend my heartfelt appreciation to my lead researcher, Dr. Bülent Arıkan, for generously sharing his extensive knowledge of solar cell fabrication processes, particularly plating and PERC solar cells. His assistance in conducting numerous experiments has been immensely valuable in advancing my research.

I am deeply thankful to Assoc. Prof. Dr. Veysel Ünsür, my metallization leader, for sharing his invaluable expertise in solar cell metallization. His guidance has greatly contributed to the success of this project.

A special note of thanks goes to our dedicated technicians, Murat, and Batuhan, , whose unwavering support has been crucial to the smooth execution of experiments and tasks throughout this journey.

I am indebted to all members of the ODTÜ GÜNAM GPVL team for their camaraderie, encouragement, and collaborative spirit, which have fostered a conducive environment for research and learning.

Finally, my heartfelt gratitude goes to my family. My parents and my brother have been unwavering pillars of support, unwavering in their belief in me. Their encouragement and love have been my driving force.

This work has been made possible through the support of the TUBİTAK 6550 project, for which I am truly grateful.

TABLE OF CONTENTS

CHAPTERS

LIST OF TABLES

TABLES

LIST OF FIGURES

FIGURES

LIST OF ABBREVIATIONS

ABBREVIATIONS

4PP	Four-point probe
Ag	Silver
Al	Aluminum
AlO_x	Aluminum oxide
AM	Air mass
ARC	Anti-reflection coating
a-Si	Amorphous Si
B	Boron
BSF	Back surface field
Cu	Copper
CZ-Si	Czochralski grown silicon
f	Frequency
FF	Fill factor
HCl	Hydrochloric acid
HF	Hydrofluoric acid
HNO_3	Nitric acid
IR	Infrared
I_{SC}	Short circuit current
I_L	Light generated current
I0	Dark saturation current

I_{MP}	Maximum current point
ITRPV	International technology roadmap for photovoltaic
J_{SC}	Short-circuit current density
k	Boltzmann constant
kHz	Kilohertz
KOH	Potassium hydroxide
LED	Light-emitting diode
LIP	Light-induced plating
LIPSS	Laser-induced periodic surface structure
MHz	Megahertz
mV	Millivolt
n	Ideality factor
nm	Nanometer
Ni	Nickel
ns	Nanosecond
P	Phosphorus
P_{IN}	Input Power
P_{MAX}	Maximum power
P_{MP}	Maximum power point
PCE	Power conversion efficiency
PECVD	Plasma enhanced chemical vapor deposition
PERC	Passivated emitter and rear cell

ps	Picosecond
PSG	Phosphosilicate glass
PV	Photovoltaics
R_C	Contact resistivity
R_{CH}	Characteristic resistance
R_S	Series resistance
R_{SH}	Shunt resistance
R_{Sheet}	Sheet resistance
SEM	Scanning electron microscopy
Si	Silicon
SiN_x	Silicon nitride
SiO_x	Silicon oxide
SiO_2	Silicon dioxide
T	Temperature
TLM	Transfer length method
UV	Ultraviolet
V	Voltage
V_{OC}	Open circuit voltage
YAG	Yttrium aluminum garnet

CHAPTER 1

INTRODUCTION

1.1 Thesis Motivation

The Photovoltaic (PV) industry aims to decrease harmful emulsions and the global average temperature by improving production capacity. According to PV roadmaps, the global market share of c-Si based solar cells will increase by this at the end of the 2033 year, and the estimated capacity for PV modules will be at least 8.5TW by 2050 [1].

Screen printing is widely used for contact formation in the solar industry due to its properties of mass and fast production capacities, but it has challenges like Ag metal prices. The rising cost of silver paste and thinner silicon wafers push manufacturers to find new metallization techniques using less silver and contactless metal formation [2]. Several approaches can be employed to decrease the consumption of silver, such as reducing the amount of silver used during the metallization by decreasing finger width and reducing the shadowing effect on the front side. However, it is limited until a certain point due to increase in series resistance. Therefore, alternative methods for metalizing silicon solar cells are crucial for higher efficiency and low cost [3], [4].

A workshop series starting in 2008 in the Netherlands has been dedicated to advancing the metallization of silicon solar cells. These efforts aim to reduce production costs and enhance efficiency [5]. Ni/Cu plating is a promising technique and a strong candidate for future contact technology. This process improves metallization with accuracy and low contact resistance while being cost-effective and suitable for mass production. It involves plating Ni and Cu onto the solar cell surface to create efficient contacts. However, Cu has to meet some crucial requirements during the deposition as the front side metal. Developing efficient, reliable, and compatible deposition techniques with existing manufacturing processes is required.

The development of plated contacts was started in Bell Laboratories in the 1950s; the first attempt at plated metal contacts on the silicon cell had the challenge of adhesion. Later, following innovations such as electroless plating of Ni seed/barrier layer resulted in the nickel silicide barriers and silver capping layers to Cu conductive layer plating method. These historical developments are detailed by Lennon *et al.* [6].

The main topic is the process complexity of Cu deposition. One of the most used techniques for Cu deposition is plating by using the electrolysis method to deposit Cu with a chemical reaction from the solution of Cu salt. Integration of large-scale manufacturing for plating is essential, and mass production tools exist. Furthermore, to be efficient, only Cu plating is not a reliable process since Cu can diffuse into the underlying c-Si layer and lead to junction shunting. Process complexity of the Cu deposition by plating technique involves the extra seed layer to eliminate diffusion of Cu into the Si and a capping layer to prevent the oxidation of Cu for durability. Therefore, replacing Ag with Cu offers cost-effective and more abundant advantages. However, to succeed in the implantation of the Cu metal contacts with an alternative to Ag, it is crucial to address challenges about the process complexity, durability, and availability for mass production is vital. By overcoming these challenges, the efficiency and cost of the metallization step can be enhanced.

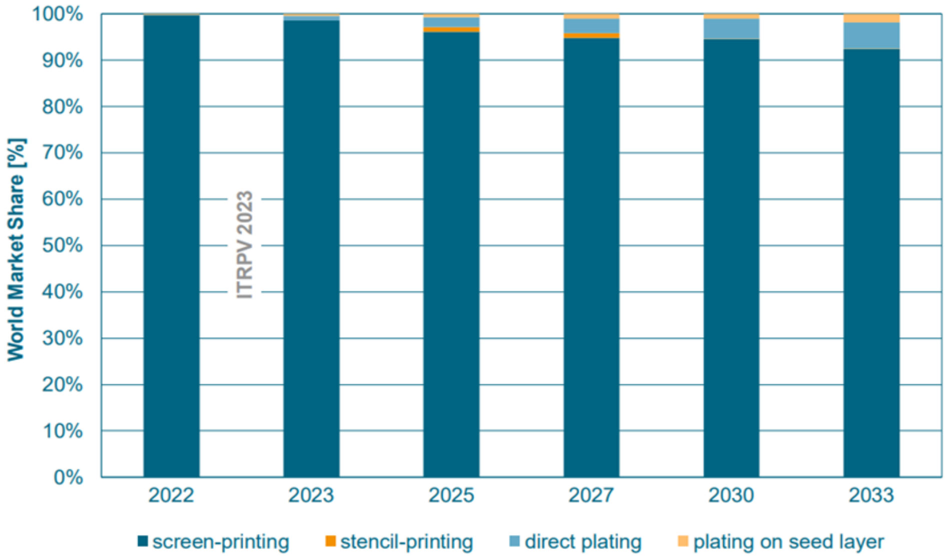

Figure 1.1 The expected market share trend of different metallization technologies for the front side from ITRPV 2023 [7].

As shown in Figure 1.1, the estimations for market share of different front-side metallization techniques are present from the ITRPV roadmap [7]. The portion shown for direct plating and plating on the seed layer is not expected to have a significant market share from 2022 to 2033. Based on the ongoing progress in plating studies, the estimated rise during these years has a significant potential to experience additional escalation. Several studies have been performed to increase the plating method market share for lower contact resistivity and higher efficiency results.

1.2 Aim of the Thesis

Nickel plating is used for semiconducting surfaces before conductive Cu layer deposition, which employs a complexing agent, buffer agent, and reducing agent to form a metal film. Light-induced electroless plating (LIEP) and light-induced plating (LIP) techniques are widely adopted, wherein the sample is immersed in a plating bath and subjected to protective potential and light to enhance plating uniformity and speed.

To obtain competitive to screen printed contacts' contact resistivity values from the plated contacts, one significant effect comes from the Ni-Si phase formation. It is known that heat treatments can form several Ni-Si phases. However, between those Ni-Si phases, Ni_1Si_1 has the lowest contact resistivity. It is also known that the Ni-Si phases can promote contact adhesion, enhancing plated contacts' durability.

This thesis aims to optimize the nickel seed/barrier layer as an excellent barrier to copper diffusion and lower contact resistivity by forming an adhesive Ni-Si interface. The nickel seed layer is deposited after opening the conductive areas on the dielectric layer by laser ablation with a precise and fast method. During the deposition of the nickel seed layer, light-induced and bias-assisted plating is introduced to grow a uniform and well-controlled contact. Given current density and deposition time, several light exposure parameters are investigated for the effect on the Ni seed layer properties. After the Ni seed layer is formed on the ablated dielectric areas, the Cu conductive layer is also deposited by the same method, and the copper diffusion during the heat treatments is checked.

This study enhances the understanding of front contact formation through the bias-assisted and light-induced plating for Ni/Cu/Ag metal stack on the laser-ablated SiNx dielectric passivation layer. The primary objectives of this thesis study were as follows:

1. To quantitatively investigate the influence of industrially feasible lasers of 1064nm ns and 532nm ps, removal of the SiN_x dielectric layer for contact openings

performed by laser ablation. This effect was conducted by observing surface modification using scanning electron microscopy (SEM), and optical microscopy. Furthermore, the quality of the Ni seed layer and underlying layer damage will give information about the effectiveness of ablation by comparing the efficiency of fabricated PERC samples.

2. To diminish the process complexity by excluding the step of chemical HF pretreatment between the laser ablation and Ni seed layer plating steps. The uniformity of the contacts was observed by surface optical imaging.

3. To acquire the aspect ratio and uniformity of contacts, plating rates were determined by giving external current densities between $1A/dm^2$ to $32A/dm^2$ for Ni seed layer deposition by plating. This assessment was analyzed by microscope images and the finger height/width ratio investigations.

4. To augment the potential for mass-scale production, Ni/Cu/Ag plated PERC solar cells were annealed with different methods, including a tube furnace, hotplate with N_2 atmospheres, and belt furnace.

1.3 Thesis Outline

Chapter 1 explains the thesis motivation and includes the significant need for an alternative to screen-printed Ag, which has dominated the PV industry for the front side of solar cells. This necessity results from the increasing cost and decreasing availability of Ag by adding extra production costs for solar cell fabrication. Appropriate references are given in this section to provide the thesis motivation for an alternative metal deposition method that is plated Ni//Cu/Ag metal stack. After the thesis motivation is mentioned, the study aims are explained step by step. Following the purposes, the thesis outline is given in this section.

Chapter 2 starts with reviewing the c-Si solar cells, emphasizing metallization techniques, PERC structure, fabrication of PERC, and basic principles with formulations given. After having overall information about PERC-type solar cells and different metallization techniques, plating is detailed in the literature reviews. The extensive knowledge of required processes before and after the plated Ni/Cu/Ag metal stack deposition is presented.

Chapter 3 presents the fabrication and characterization techniques for the analysis of samples. Followed by the laser ablation, plating of Ni, Cu, and Ag to the annealing of samples is determined in the fabrication part. In the characterization part, optical (SEM and optical microscopy) and electrical characterization (IV curves, SunsVoc, and TLM) methods are given to analyze the completed Ni/Cu/Ag plated PERC solar cells.

Chapter 4 defines the results and discussion after performing the experiments and characterizations. The effects started by laser ablation of the dielectric layer, and optimum lasers and laser parameters are chosen by examination of surface morphology and deposited metal qualities. Then, with optimum laser ablations, light-induced bias-assisted plating is performed for each part of the metal stack as a seed layer of Ni, a conductive layer of Cu, and a capping layer of Ag. Controllable parameters and their effects on contact quality are indicated during plating. Lastly, samples are annealed with different temperatures for the contact formation to introduce the heat and time effects on solar cell efficiencies.

Chapter 5 concludes with this thesis study's essential results and summarizes future research to improve the obtained results.

CHAPTER 2

THEORETICAL BACKGROUND

2.1 Development of Solar Cells

From the beginning to the last world record, solar cells in lab-scale efficiency will be mentioned in this part, emphasizing the progress of metallization techniques. In 1941, the US patent announced the first solar cell with electroplated rhodium contacts; however, the cell efficiency was below 1%. In the 1950s, Bell Laboratories achieved an efficiency above 10% by single crystal growth, formation of a p-n junction with lithium and boron diffusions, and plated rear rhodium contacts. Plated back rhodium contact does the connections for module applications; however, the contact resistivity values were high. In the 1970s, COMSAT Laboratories achieved efficiency values over 15% by evaporating rear side Al contacts that construct the heavily doped p+ region and decreasing the recombination at the backside. In 1985, UNSW developed a new passivated emitter solar cell (PESC). The PESC opened the silicon oxide passivation layer by photolithography for the front evaporated/plated Ti/Pd/Ag contact. Later, PESCs had efficiencies above 20% through the texturing design of microgrooves and float-zone B-doped c-Si wafers. After that, in early 1988, at Stanford University, interdigitated back contact (IBC) solar cell design was invented with 22% cell efficiency by focusing on the rear side passivation qualities and heavily diffused contacts underneath to reduce recombination and resistive losses, respectively. Afterward, in 1999, UNSW designed PERC and PERL solar cells with an efficiency of 25%.

Nonetheless, the industry achieved 24% PERC solar cell efficiencies 20 years later with larger-size Cz-Si substrates. TOPCon solar cells are reported by Fraunhofer ISE as having 26% efficiency with front Ti/Pb/Ag contacts on p-type FZ c-Si substrates. Lastly, the world champion polycrystalline on oxide IBC cell is introduced by ISFH.

Those mentioned cells were on the lab-scale studies; however, to be industrially feasible and available to mass production, those lab-scale studies should be converted to less complex, robust, cost-effective processes.

To summarize, the evolution of solar cell technologies has seen the development of various innovative approaches to enhance efficiency. The journey began with Al-BSF (Aluminum Back Surface Field) cells in the early days of solar cell development, where companies like SunPower contributed to the concept of utilizing a textured front surface and an aluminum rear layer to improve carrier collection. Subsequently, the focus shifted to PERC (Passivated Emitter Rear Contact) cells, pioneered in the mid-2000s and championed by companies such as Trina Solar and JinkoSolar, replacing the emitter to the rear side to decrease recombination losses and significantly improving efficiency. Building upon PERC, PERL (Passivated Emitter Rear Locally-diffused) cells emerged, with entities like Fraunhofer ISE with localized diffusion on the rear side to further improve carrier collection. In parallel, Panasonic led the development of TOPCON (Tunnel Oxide Passivated Contact) cells, introduced in the late 2000s, with the interaction of thin silicon oxide layers for passivation and efficient carrier transport. Lastly, IBC (Interdigitated Back Contact) cells, pioneered by companies like SunPower and Panasonic, were developed around the same time, introducing contacts on the rear side in an interdigitated pattern, reaching high efficiency particularly crucial for space applications.

This first section presents solar cell developments to understand the critical features of the solar cell concept. Then, the currently dominating solar cell type of passivated emitter rear contact (PERC) will be explained by its fabrication procedures, structural design, and the principle of operation in the next section.

2.2 Development of PERC

2.2.1 Operation Principle and Fabrication of PERC

PERC solar cell structure forming starts with a p-type c-Si substrate, and to eliminate the impurities after slicing the ingot into wafers, saw damage etching is performed. To decrease the reflection by constructing the triangle pyramids on the c-Si substrate via texturing is done. Phosphorous (P) doping by diffusion furnace is completed, and a p-n junction is created to separate the photo-generated electron-hole pairs in the cell. Undesired rear side P is removed by single side etching (SSE) by RENA inline tool. Passivation is achieved both with Al_2O_3 and SiN_x layer depositions by ALD and PECVD tools. A front anti-reflection coating is done on the front surface to increase the amount of captured light in the cell. Rear local contact openings for Al BSF are managed with 532nn ps laser, and front Ag and rear Al metal contacts are printed with an industrial scale production screen-printer. The fast-firing oven is used for temperature treatment to activate the passivation and form the metal contacts. In Figure 2.1 and Figure 2.2 process steps and device structure can be seen. Also, the detailed fabrication steps are explained in the subsections.

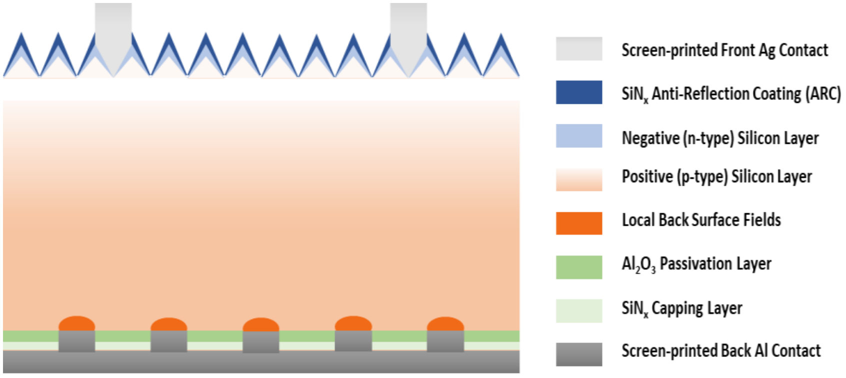

Figure 2.1 PERC type solar cell structure.

Figure 2.2 PERC Fabrication steps.

2.2.1.1 Saw-damage etching (SDE)

After cutting ingots into the wafers by the sawing process, the surface is damaged, and some residual contaminations are introduced to the wafer surface. Chemical treatment with NaOH, KOH, or TMAH solutions is applied to etch the damaged layer around 5-10um and leave a clean surface before going through other production processes. The etch rate of the wafer surface mostly depends on the concentrations of $[OH^-]$ and $[H_2O]$ in solutions. In this step, determining the etching rate plays a critical role since over-etching can cause wafer breakage during the further production steps, and under-etching can reduce the solar cell's performance by lowering the minority carrier lifetime due to remaining contaminations.

2.2.1.2 Texturing

In the SDE process, the wafer surface is smoothened, increasing the surface refelection and decreasing the chance of bouncing back the light beam to the cell.

Texturing is an etching step to create pyramids in the silicon surface to reduce the reflection from the surface, which can be seen in Figure 2.3. The different types of the silicon wafer, such as monocrystalline and multi-crystalline c-Si wafers, show other behavior with texturing chemicals. For example, on the monocrystalline surface with <100> orientation, texturing is generally done by NaOH, KOH, or TMAH, with IPA or organic additives to create random pyramids. The etching rate of alkaline etchants is much higher for the <100> (pyramid base) than the <111>(pyramid face) orientated c-Si surface. Hence, anisotropic etching builds up the upright pyramidical shape on the etched c-Si surface. The textured surface orientations can be seen in Figure 2.4.

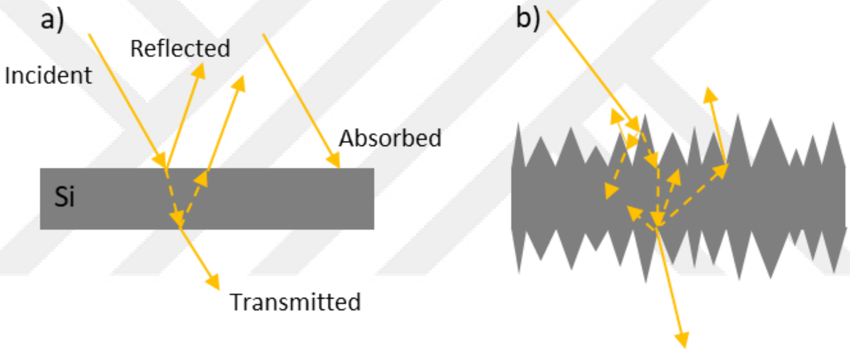

Figure 2.3 Si surface light reflections with rough (left) and textured surfaces (right).

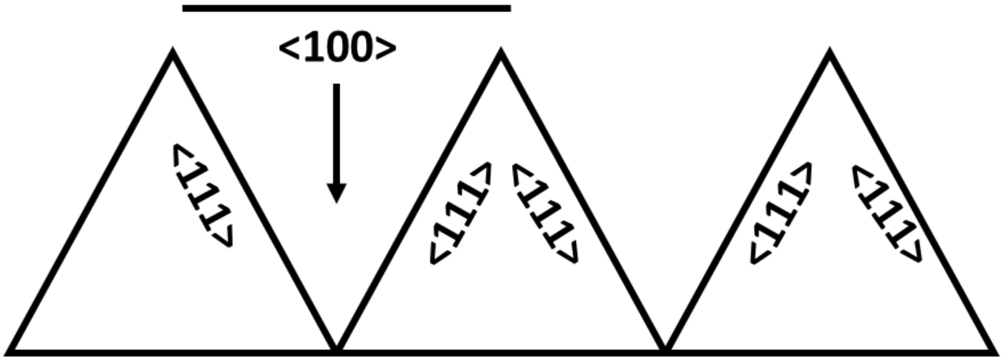

Figure 2.4 c-Si surface etching orientations.

2.2.1.3 P Doping

Phosphorous doping is performed to form an n^+ emitter for p-type c-Si-based solar cells by $POCl_3$ diffusion. POCl3 diffusion includes two phases: phosphosilicate glass (PSG) layer deposition and drive-in the P atoms deeper inside the Si substrate. During the process, temperature and gas flows are controlled to conformal P doping.

2.2.1.4 Single Side Etching (SSE)

During the P doping, the PSG layer is formed on both the wafer's front and rear surfaces and edges. Single-side etching is required to eliminate the recombination of minority carriers and increase the internal reflection from the rear side of the solar cell. The single-side etching process includes HF, H_2SO_4, HNO_3, and DI water solution. In the RENA InPilot tool, wafers are placed on the rear side facing the etchant solutions, which removes the PSG layer, and the front side is protected with DI water not to affect the n-doped region and pyrmides on the front surface.

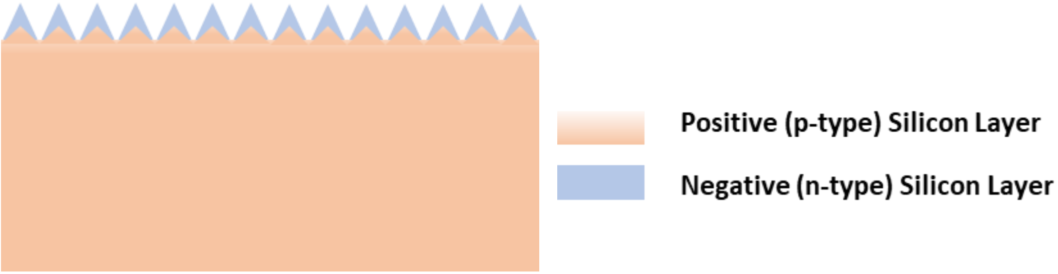

Figure 2.5 Schematic representation of p-type c-Si with n-type emitter after single-side etching.

2.2.1.5 Rear: Al_2O_3 Deposition

The atomic layer deposition (ALD) tool is used to deposite a nanoscale-thick aluminum oxide (Al_2O_3) layer around a few nanometers as a passivation layer. ALD is a particular type of chemical vapor deposition (CVD) that contains the TMA, DI-water, and N_2 vapors and forms the monolayer of Al_2O_3 atoms by chemisorption. The Al_2O_3 deposition cycle is repeated to get the desired thickness by introducing the gases again to deposit a second or more layers. Ultimately, a temperature treatment is applied to stabilize the Al_2O_3 layer.

2.2.1.6 Rear: SiN_x/SiO_xN_y Capping Layers Deposition:

After the Al_2O_3 passivation layer, a second passivation layer of SiN_x: H is deposited as a capping layer on a thin Al_2O_3 layer by direct plasma enhanced chemical vapor deposition (PECVD) reactor at low frequency and temperature (450°C). The precursor gases sent to the reactor during the SiN_x/SiO_xN_y thin film depositions are silane (SiH_4), ammonia (NH_3), nitrogen(N_2), nitrous oxide (N_2O), and various gas flows that can be used to modify film properties. Passivation quality at the rear side of c-Si solar cells is enhanced by Al_2O_3/ SiN_x: H stack.

2.2.1.7 Front: ARC Deposition:

The SiN_x/SiO_xN_y layers are widely used as ARC & passivation. Two critical optimizations are needed to reduce reflection and defect centers in the surface and bulk. The refractive index and thickness of the anti-reflection coating (ARC) are arranged to minimize the reflection of the light from the surface. The dangling bonds in bulk are passivated by H atoms introduced by deposited layers after the heat treatment.

2.2.1.8 Rear: Local Contact Opening:

Before the aluminum metallization, it is required to open the passivation Al_2O_3/ SiN_x: H stack by a 532nm wavelength ps laser. Several parameters of wavelength, pulse duration, frequency, power, and scan speed are investigated to ablate the passivation layer on the rear side. Locally opening the passivation stack to construct an Al back surface field (BSF) at the rear side, laser ablation parameters are essential in the contact quality, shape, and thickness. For example, laser power affects the opened area width and determines the metal adhesion; laser wavelength impacts the absorption depth of the light on the Si surface; laser pulse overlapping can be arranged so as not to damage the underlying surface severely. More details about the laser parameters will be given in the front LCO Section 2.3.4.1.

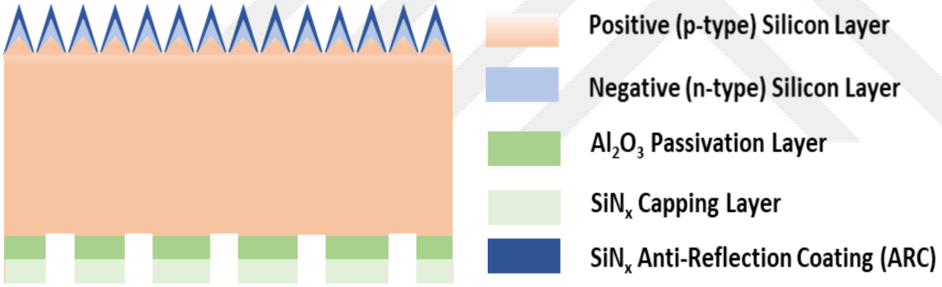

Figure 2.6 Schematic representation of p-type c-Si with the n-type emitter, Al_2O_3, SiNx, and SiNx ARC passivation layers after locally opening the rear passivation layers by laser ablation.

2.2.1.9 Screen Printed Al and Ag Metallization:

The screen-printing method has three phases: 1) the fill phase, 2) the contact phase, and 3) the release phase. Firstly, the squeegee fills the screen with the paste, and the screen contacts the substrate. Then, the paste is forced through the designed pattern of the screen to install the paste on the substrate. Finally, the squeegee and screen pressure are removed from the surface by leaving a fine metal grid on the substrate.

Screen printing has several components which can affect the metallization results. These are screen design, paste content, substrate, printing speed, squeegee pressure, and distance between screen and substrate.

Aluminum is the most used metal for rear side metallization technique with the screen-printing method due to creating BSF region. The back side of the solar cell is ablated by laser to create local BSF regions where Al interacts with Si. This BSF region acts as a highly doped p+ region to decrease the recombination at the rear side when the Al-Si alloy is obtained with sintering.

Ag front metal is deposited on the front side with the screen-printing method, the same as Al. The only difference is the screen design of the mask, which has fingers and a busbar instead of total coverage of Al at the backside. The front grid design has optimum thin fingers and busbars on the surface to collect electrons from the n+ emitter side with minimum shading effect.

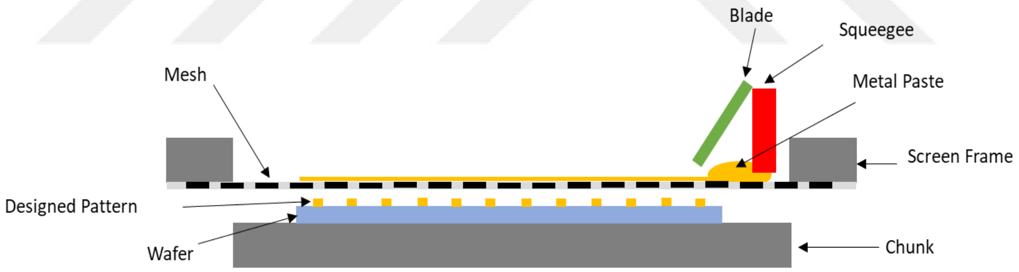

Figure 2.7 Schematic representation of screen printing.

2.2.1.10 Contact Formation via Fast Firing Furnace:

A fast-firing furnace is used for three main reasons: forming rear side Al contact, front side Ag contact, and decreasing the number of dangling bonds and trap states by passivation of H comes from the SiNx:H layer.

A fast-firing furnace has several temperature zones that can be arranged with optimum T values to get the best results. Also, the profile of the zone temperatures can be analyzed to obtain good adhesion, low series resistance, and high FF [8].

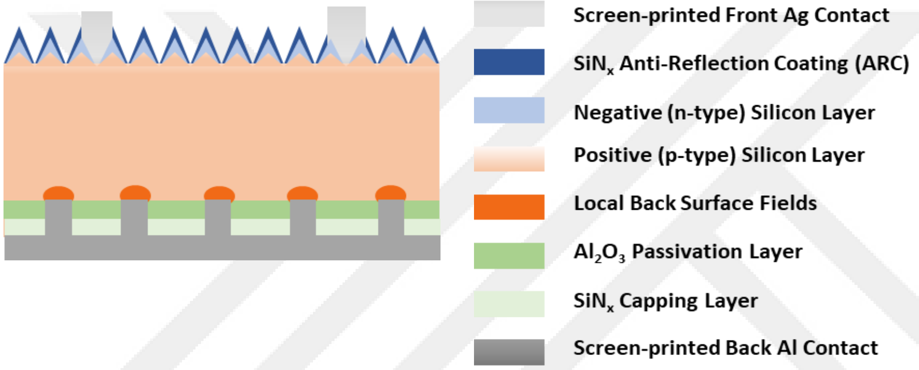

Figure 2.8 Schematic representation of p-type c-Si with the n-type emitter, Al$_2$O$_3$, SiN$_x$, ARC passivation layers, rear Al-BSF, and front Ag-screen printed metals after contact formation.

After providing information about the PERC structure and the essential fabrication steps, the next step involves grasping the operational principles of the solar cell mechanism. This foundational understanding sets the stage for exploring the basic equations that define its behavior, which will be covered in the following section.

2.3 Basic Principles of Solar Cells

When the electron is excited to the conduction band, it leaves a space called a hole in the valance band. The p-n junction will separate these photo-generated electron-hole pair before it recombines, and those separated electrons are collected as a photo-generated current out by the metal contacts. To determine the behavior of the solar cell under illumination and in the dark can be analyzed by the IV curve that gives basic solar cell parameters such as V_{oc} V_{mp} I_{mp} I_{sc} and FF.

First, the one-diode or ideal diode equation can be expressed as:

1

$$I = I_0\left[exp\left(\frac{qV}{nkT}\right) - 1\right] - I_L$$

where I_0 is the saturation current under no illumination, q is the electron charge, V is the voltage, n is the ideality factor, k is the Boltzmann constant, T is the temperature, and IL is the light-generated current.

I_{SC} is the short-circuit current through the solar cell when the cell is short-circuited at zero voltage across the cell and comes from the generation and collection of charge carriers.

Open circuit voltage is the maximum voltage extracted from the diode equation when no current passes through the cell.

2

$$V_{OC} = \frac{nkT}{q} \times \ln\left(\left(\frac{I_L}{I_0}\right) + 1\right) \approx \frac{nkT}{q} \times \ln\left(\frac{I_L}{I_0}\right)$$

The fill factor measures the squareness of an IV curve and represents the maximum rectangle under the IV curve. The importance of the FF lies in the relation between maximum power, I_{SC}, and V_{OC}. Therefore, FF can be formulated as:

3

$$FF = \frac{V_{MP} I_{MP}}{V_{OC} I_{SC}} = \frac{P_{MAX}}{V_{OC} I_{SC}}$$

Where V_{MP}, I_{MP}, P_{MAX} are maximum voltage, current, and power points, respectively.

The power conversion efficiency of a solar cell can be described as the fraction of input power that is transferred to electricity obtained from the device and formulated as:

4

$$P_{MAX} = V_{OC} I_{SC} FF$$

5

$$\eta = \frac{P_{MAX}}{P_{IN}} = \frac{V_{OC} I_{SC} FF}{P_{IN}}$$

where η is the efficiency of a solar cell, P_{IN} is the input power, and equals 1kW/m^2 under the conditions of AM1.5 spectra and at the temperature of 25℃.

The current-voltage (I-V) curve showcases the relationship between the generated current and the voltage across the terminals of the solar cell. At zero voltage (short circuit condition), the solar cell operates with a maximum current flow named I_{sc}, representing the maximum current obtained from the cell when there is no resistance in the external circuit. When there is no current flow (open circuit condition), the solar cell operates with a maximum voltage known as V_{oc}, which is the potential difference across the terminals when there is no current. The point where the I-V curve intersects the y-axis (current axis) is the short circuit current (I_{sc}), and the point where it intersects the x-axis (voltage axis) is the open circuit voltage (V_{oc}). At the maximum power point, the product of voltage and current is at its highest, representing the maximum power the solar cell can deliver to the external circuit. These values are critical in evaluating the performance of a solar cell. The I-V curve shown in Figure 2.17 provides valuable insights into how a solar cell behaves under different operating conditions, helping us assess its efficiency and effectiveness in converting sunlight into electrical power.

In a PERC solar cell, series resistance components introduce losses that hinder current flow, impacting the cell's efficiency. These resistances can be expressed using Ohm's law. Front Contact Series Resistance (R_f) arises from the front metal grid and emitter region, where V is the voltage drop across the contact and I is the current passing through it. Emitter Sheet Resistance (R_s) accounts for the resistance in the lightly doped emitter region. A higher Rs leads to more voltage drop. Base Series Resistance (R_b) is the resistance in the silicon base material for the current flowing through the base. Back Contact Series Resistance (R_c) represents resistance at the back metal contact. Metallization Contact Resistance (R_c) quantifies the resistance at the metal-to-silicon interface. These resistances reduce the cell's output current and voltage, impacting power conversion efficiency. Minimizing them is vital for optimizing solar cell performance.

After mentioning the resistive components, the metal process related to the back contact resistance and metallization contact resistance concepts will be understood more clearly with different metallization technique presentations in the next section.

2.4 Metallization Techniques of Solar Cells

Solar cells need metal electrodes to collect the photo-generated current from sunlight exposure. These electrodes are usually deposited on the front and back sides of the cell using different methods like evaporation, printing, or electroplating. The electrodes must meet some requirements: minimal shading for the front side mono facial cells and the back side bifacial solar cells, adhesive to the underlying layer, lower contact and series resistances, and recombination velocities between metal-semiconductor. Those requirements must be considered while designing the metal grids depending on the metallization technique used. High-efficiency solar cell achievement depends on the high-quality metal of the solar cell since the series (R_{series}) and shunt resistances (R_{shunt}), ideality factor (n), reverse saturation current (J_{02}), fill factor (FF), open circuit voltage (V_{oc}) values are affected by the front and rear contacts.

There are several main approaches to getting contact from the industrial c-Si solar cell: evaporated, screen printed, alternative printing, and plated contacts. In the following sub-sections, plating will be given in detail in the scope of this thesis study.

2.4.1 Evaporation of Metal

Evaporation of metal for deposition uses the physical vapor deposition (PVD) process. The PVD process can be divided into three steps: solid-to-gas conversion, transferring the evaporated gaseous metal atoms to the substrate surface, and condensation of metal on the substrate surface by nucleation and film growth. The evaporation system is illustrated in Figure 2.9. The essential components are a chamber, vacuum pumps, instrumentation, and metal source heater. Samples are placed on the rotating holder on top of the metal source. The heated metal source is melted and vaporized in the chamber. High vacuum condition is required around 10^{-6} mbar by a combination of different vacuum pumps to direct metal atoms and minimize the contamination and collisions of metal atoms. Metal heating can be done by resistive (thermal evaporation), laser heating, and electron bombardment (e-beam evaporation) heating. The system's instrumentation gives information about the deposition rate and vacuum level. Therefore, vaporized metal atoms are directed to the substrate surface to form a solid, thin metal layer.

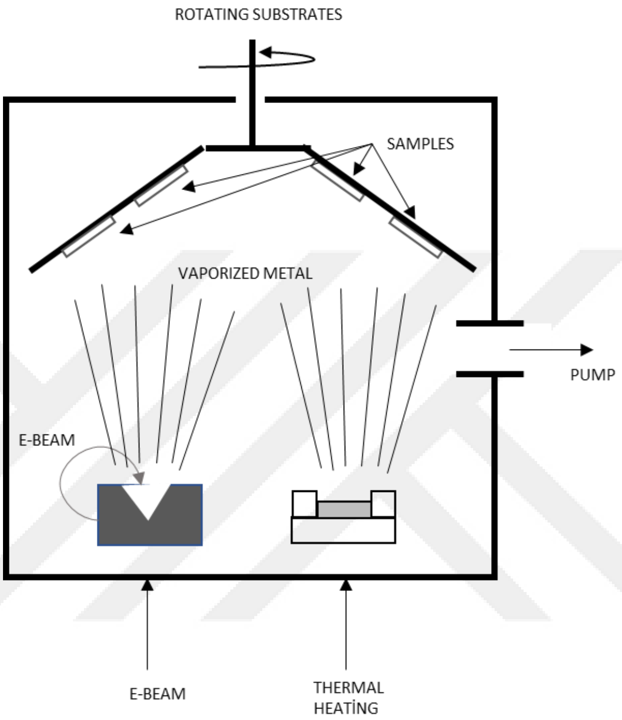

Figure 2.9 Metal deposition systems with e-beam and thermal heating methods.

Another type of metal deposition is sputtering. The sputtering method uses plasma energy to pull the target metal atoms toward the sample surface. Metal target is considered as cathode and sample holder as an anode. Metal target is bombarded with pure, noble gas ions (Ar^+) in the vacuum chamber. To create an Ar^+ plasma bombardment, a high voltage is applied between the anode and cathode. These ejected metal ions are condensed on the sample surface to form the metal-deposited film. The schematic representation of the sputtering can be shown in Figure 2.10.

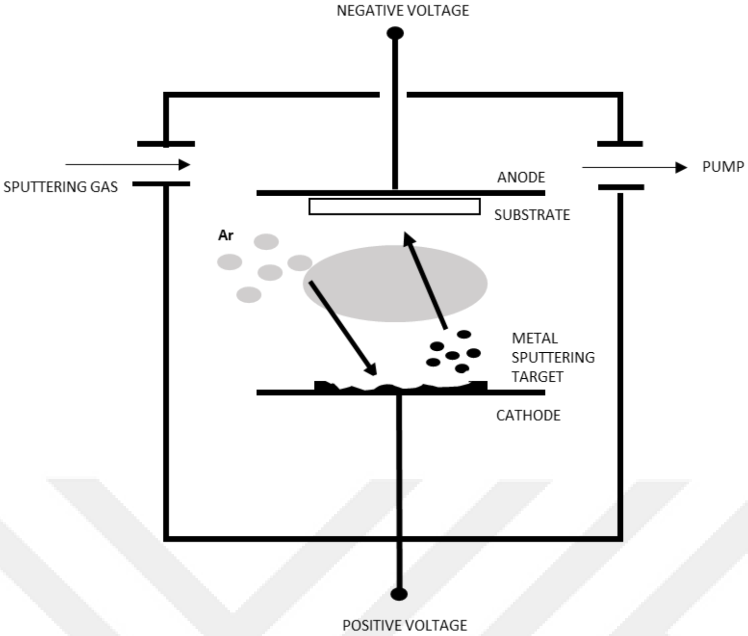

Figure 2.10 Schematic representation of DC sputtering system.

However, those metallization techniques have some disadvantages that damage the sample surface, reduce the passivation quality, create spikes in the material, and are unsuitable for mass production and complex pre-structuring. Laser ablation, electrochemical deposition, and printing technologies are more popular due to their straightforward process structuring and mass production properties.

2.4.2 Alternative Printings

This part will discuss several alternative printing techniques, such as parallel dispersing, rotary printing, and laser transfer printing.

2.4.2.1 Parallel Dispensing

Especially for fragile samples, the parallel dispersing technique is favorable since the only contact is the functional medium (or metal paste), referred to as contactless deposition. The dispersing system includes a nozzle fill of active medium. Depending on the desired pattern, the medium is forced through the nozzle opening and deposits dispensed metal grids as dots or lines for both the front and back sides of the solar cells. The advantages of using less metal paste, homogenous deposition without mesh marks, and high throughput for future applications are demonstrated.

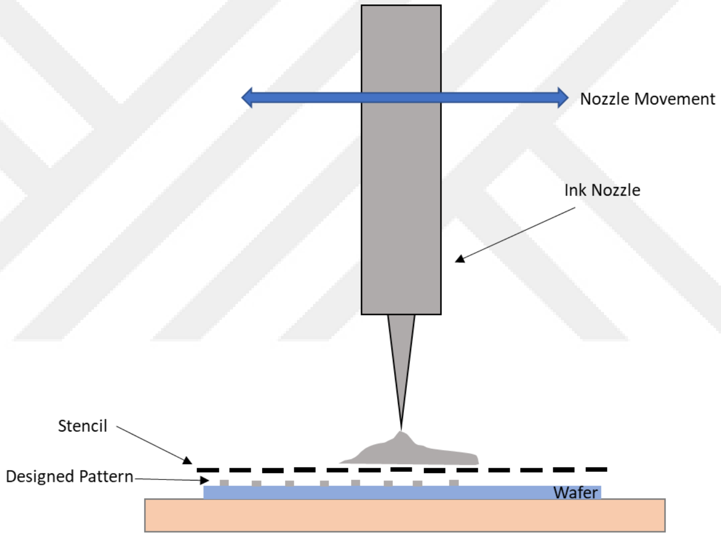

Figure 2.11 Scheme of stensil printing tool.

2.4.2.2 Rotary Printing

Rotary screen printing (RSP) is considered the thick film printing tool with a printing velocity of 160m/min [9]. When certain paste-like liquids are modified to have suitable rheological properties, they can be printed using RSP, which opens up opportunities for high-productivity printing in various fields. Besides traditional areas like graphic arts and textile printing, RSP can also be used for technical printing functions like flexible solar cells [9],[10], RFID antennas [11], and conductive circuits [12]. However, RSP machines are more complex, large, and cost-intensive than flat-screen printing machines, which are more straightforward and do not require roll-to-roll or roll-to-flat printing. Compared to flatbed screens, rotary screens have a greater wire thickness, allowing higher stability during printing. The wire thickness for rotary screens is typically around 30-60 µm to ensure sufficient stability, which is substantially thicker than flatbed screens. This thickness reduces the percentage of the open screen surface. As a result, RSP is suitable for mass production, as opposed to small-scale laboratory applications.

The rotary screen can be made of either a woven mesh of fine wires, usually of stainless steel, or structured nickel foil cylinders with a hexagonal honeycomb structure, referred to as the rotary stencil. The screen of the rotary cylinder is filled with a metal paste, which is transferred to the wafer through the mesh openings with squeegee pressure. Figure 2.21 shows the schematic drawing of the RSP tool. Other than optimum screen design, such as mesh size specification, printing parameters, metal paste, squeegee, and substrate must be optimized to obtain the desired printed metal of the solar cell.

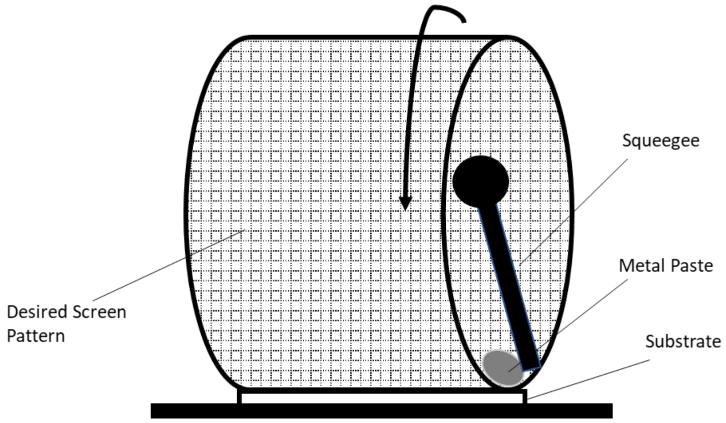

Figure 2.12 Schematic view of a rotary screen-printing unit.

2.4.2.3 LIFT Printing

The laser-induced forward transfer (LIFT) technology is a type of laser printing that falls under the additive direct laser printing or laser writing methods category. A transparent material (donor) is coated with the layer that needs to be transferred to perform the LIFT process. Afterward, a laser beam transfers the layer onto a substrate (target) like a solar cell as seen in Figure 2.22. The LIFT process can transmit structured materials, such as organic materials, ceramics, and metals, in solid, paste, or liquid forms [13].

On the other hand, the donor coating plays a vital role in the LIFT process as it needs to absorb the laser radiation and transfer the metal to the target substrate. The donor coating also needs to have good adhesion to the donor material and should not cause any damage to the target substrate. Lastly, the target substrate is also important as it needs to be able to withstand the intense laser radiation and allow the transferred metal to adhere to its surface. The target substrate also needs to have compatible properties with the metal being transferred in terms of thermal expansion coefficient, adhesion, and conductivity. Te LIFT process for metals requires careful consideration of the interplay between the laser, donor material, donor coating, and target substrate to ensure successful metal transfer and proper adhesion to the target substrate [14].

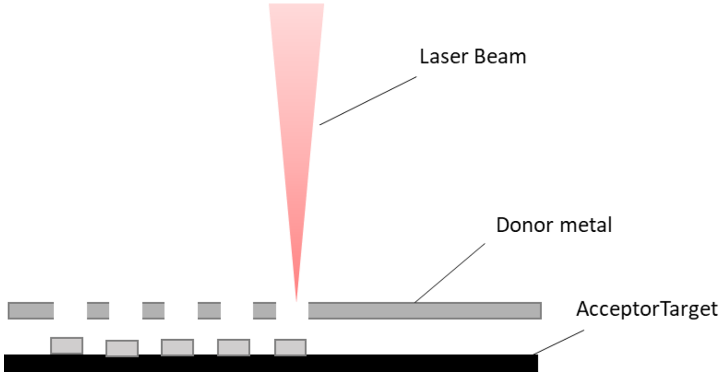

Figure 2.13 Schematic illustration of LIFT.

2.4.3 Screen Printing

Printed contacts are the most commonly used method for metallization in the production of solar cells due to the speed and simplicity of printing systems. Creating contacts takes less than one second per wafer and is becoming even faster. Photolithography, commonly used in microelectronics, is not feasible for solar cell processing due to its time-consuming nature. The most popular technique for solar cell production is still screen printing using thick film pastes.

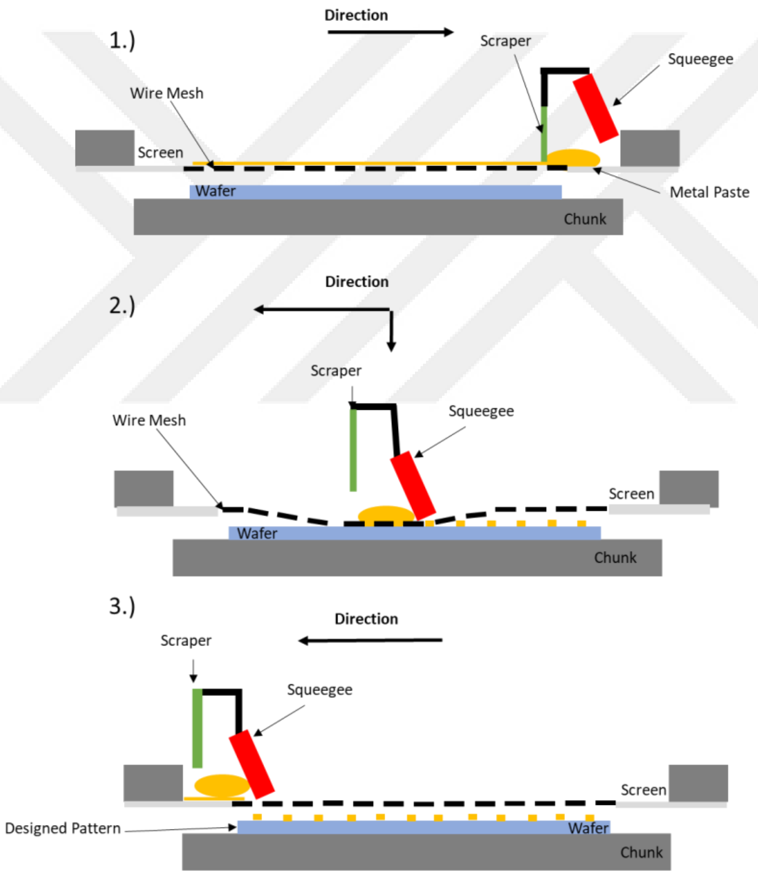

Figure 2.14 Three phase of screen printing 1.) filling, 2.) contact, 3.) release.

The operation of a squeegee in the context of printing involves its application to push printing paste through a screen onto a substrate. The technique is carried out by positioning the squeegee at a particular angle that does not exceed 90° to the screen. That allows the bulk of the paste to adopt a downward velocity as it traverses the screen, thereby promoting its flow into the opening units of the metal mesh. Throughout this process, the screen remains situated at a specific distance from the substrate, referred to as the "snap-off distance," as the squeegee does not exert any impactful forces upon it.

In the fill phase, the screen is covered with the metal paste by the scraper placed in front of the squeegee. In the contact phase, following the flooding of the mesh by the squeegee, a subsequent motion of the squeegee initiates the actual printing process. During this phase, the squeegee applies a defined amount of pressure on the screen, causing the paste to be pushed onto the substrate via the opening channel of the emulsion layer. As the squeegee moves further across the screen, the pressure behind it decreases, and due to the tautness of the mesh, the screen separates from the substrate. The contact area between the substrate and screen is called the cling zone, which varies according to the strength of paste adhesion to the screen and the mesh's restoring forces. The screen-printing machine operator must minimize the length of the cling zone by selecting suitable parameters such as squeegee velocity, snap-off distance, and screen-and-paste parameters to avoid any undesirable process instabilities. Finally, in the release phase, the pressure of the squeegee ends, and the distance between the screen and substrate is increased by leaving the paste on the substrate.

2.4.4 Plating

Plated contacts consist of various layers designed for specific purposes. The seed layer facilitates electrical contact with the semiconductor substrate, while the conductive layer uses high-conductivity materials for current conduction. The capping layer enhances the module's durability and integration within systems. Including various layers allows for flexibility and customization of contacts to suit specific usage requirements.

Metal-plated contacts are obtained through an electrochemical deposition technique. An electrolyte containing metal salt coats the electrode with its metal, with ions and counter ions present when the metal salt dissolves in the solution. Electrons are supplied from the sample to discharge the metal ions, depositing a metal layer on the electrode sample surface. Electron supplements can occur through various means, including providing external current or voltage to the sample, substrate treatment by light, or dissolving the sample surface to create chemical reactions between the electrolyte and electrode.

In electroless plating, the sample acts as a catalytically active side and dissolves the reducing agent to provide electrons for discharging metal ions in the electrolyte. Reducing agents may include doped silicon and other metal layers existing on the surface. Although it is a straightforward process, plating rates are typically slow, with several micrometers requiring a long time for deposition. Meanwhile, light-assisted electroless plating involves shining semiconductor sample surfaces with a halogen lamp, using internally generated electrons to discharge metal ions in the electrolyte. Deposition rates are affected by light properties such as wavelength and intensity, making this a relatively faster and more controllable process relative to electroless plating. Those mentioned electroless plating methods are generally used to depose a thin layer to increase the contact adhesion or behave like a barrier to disable shunting due to the upper diffusive metal layers in the bulk material.

Another type of plating is electroplating or bias-assisted plating, which uses an external current or voltage source to give electrons from the electrode to the electrolyte. In bias-assisted electroplating, electrons supplied from the sample surface reduce positively charged metal ions for metal layer deposition. The anode (metal salt ionized into the positive metal ion Me^{x+} and negative counter ion xe^{-}) is connected to the electrolyte's positive terminal. In contrast, the negative terminal is connected to the workpiece (cathode). In the cathode part, extracted electrons from the anode pass through the electrode, and a reduction reaction occurs by taking electrons formulated as $Mex^{+}+xe^{-}\rightarrow Me^{0}$ to stabilize metal ions on the cathode. Bias-assisted electroplating is relatively faster and controllable than other methods like PVD. The combination of light-induced and bias-assisted methods may also be preferable in uniform fast deposition rates.

The given current values are usually expressed as the current density with a unit of either ampere per square decimeter (ASD) or mA/cm^2 since it is proportional to the electrode surface. The electrochemical deposition rate of a metal is proportional to the amount of charge passed through the electrode. Therefore, the theoretical mass of a metal ($m_{theoretical}$) deposited to the electrode surface can be calculated by using Faraday's law:

6

$$Q(coulombs) = nF \times N$$

7

$$m_{theoretical} = \left(\frac{M}{nF}\right) Q$$

where N is the Avogadro number, M is the molar mass of deposited metal, n is the number of electrons, and F is the Faraday constant (96.484 C/mol). This formulation can calculate the amount of metal mass for a specific plated metal type. However, $m_{theoretical}$ value stands for the contribution of each electron to the deposition for homogeneous coverage. With the actual mass (m_{actual}) which is always less than $m_{theoretical}$, plating efficiency (W) can be calculated as:

8

$$W = \frac{m_{actual}}{m_{theoretical}} \times 100\%$$

The rate of heterogeneous reaction in terms of current, I, can be derived from the Faradays law as

9

$$I(amperes) = \frac{dQ}{dt}(Coulombs/s) = nF\frac{dN}{dt}$$

10

$$Rate(mol.s^{-1}) = \frac{dN}{dt} = \frac{I}{nF}$$

11

$$Rate(mol.s^{-1}cm^{-2}) = \frac{I}{nFA} = \frac{J}{nF}$$

where A is the electrode surface unit area, and J is the current density (A/cm^2).

Those formulations can express the essential electrochemical deposition basics, while the realistic reactions can occur more complexly in the aqueous solution of electrolytes. Moreover, plated metal characteristics depend on the plating tool, plating conditions (temperature, pH, light or current densities, and time), electrolyte, and electrode.

The most used metals for plating are Copper (Cu), Silver (Ag), Nickel (Ni), Tin (Sn), Zinc (Zn), Cobalt (Co), and Gold (Au) since they are available for the use of aqueous electrolytes by having the potential of electrochemical metal deposition within the water.

The main reason for selecting Ni as the barrier layer is the ability to form Ni-Si phases during the temperature treatments, and that ability reduces contact resistivity. That decrease in the contact resistivity can be investigated by TLM measurements with different temperature-implied samples.

After the Ni seed layer is formed, diffusion of the Cu atoms is avoided through the underlying layers. Cu is deposited as the conductive part of the contact. Moreover, to stabilize the contact quality, a capping layer is introduced into the process steps to eliminate the oxidation of Cu. Therefore, three different Ni/Cu/Ag metal stack is deposited for the front side contact. Ni/Cu/Ag deposition needs a conductive opening on dielectric passivation layers to electrochemical deposit by a plating method. Several methods exist for opening dielectric layers, such as photolithography, masking, or laser ablation. The two most essential methods of contact openings on the dielectric layer will be mentioned in the next section under wet chemical etching and laser ablation subtitles. Also, the reason for using laser ablation in this study is indicated by its advantages over other methods.

2.4.4.1 Patterning the dielectric layer

Current flow barriers, such as the dielectric layer, disable the electron exchange between the solar cell and electrolyte. Removal of passivation layers will modify the near-surface and create a pathway for metal deposition. It can also affect surface oxidation, roughness, and doping density. When removing dielectric layers, surface modifications, opening width, and positions are significant. Contact openings limit the requirement of minimum shading effect, so the contact opening width should be narrow without damaging the underlying layers. The other considerable requirement is precisely opening the contact positions since the contact grid needs to be aligned for diffused selective emitter applications and electrical characterizations. Thus, the removal of the dielectric layer should be precise to determine the plated metal position or grid design. Two main methods for locally opening the dielectric layer are wet chemical etching and laser ablation before the plating process.

2.4.4.1.1 Wet chemical treatment

The mask-etch method is usually used for lab-scale applications since mass production capacity is unavailable due to process complexity and cost. However, removal can be done with less damage on the underlying layer by precisely positioning the contacts. The photolithography method applies the etching mask to several um-width openings with high resolution, precision, and controllability. During the chemical treatment, etch resistive masks are used to avoid damage to the passivation layers except for contact openings. The thickness and density of the etch resistive mask should be convenient to not over or under-etch the dielectric layer.

2.4.4.1.2 Laser Ablation

Laser processes are becoming more popular for patterning dielectric layers because they are fast and accurate. However, conventional solid-state lasers with a pulse duration of ns can damage the silicon underneath. In contrast, ultra-short pulsed lasers with pulse durations of fs and ps are promising because they can selectively remove dielectric layers without damaging the silicon. Despite this promise, the mechanisms behind using these ultra-short pulsed lasers are not fully understood [15].

Several laser systems are applied to remove the dielectric layer with various parameters such as wavelength, pulse duration, and pulse energy. Laser matter interaction can be explained depending on the time frame involved. When the material absorbs the laser beam, photon energy is transferred to existing free electrons, which then oscillate and pass the energy onto other electrons and eventually to the lattice. Suppose the pulse duration of the laser beam is shorter than the electron cooling time. In that case, ions will receive the electron energy quickly enough to break their lattice bonding without leading to heat transfer. Breaking bonds without heat transfer happens in the femtosecond regime. If the pulse duration is longer than one nanosecond and thermal equilibrium is reached between the electron and lattice, heat diffusion-dominated energy loss occurs where the material melts and evaporates. In the ps regime, an intermediate regime exists between the nanosecond and femtosecond regimes. Lastly, if the pulse duration is over one millisecond, the process can be modeled by classical heat transfer. Thermal diffusivity and pulse duration can calculate the material heat-affected zone. The absorption coefficient, a measure of the penetration depth, determines how deep the photon beam will penetrate. The penetration depth of the laser pulse, L_D, can be calculated from the below equation. Also, L_D can determine the heat-affected zone in the material.

12

$$L_D = \sqrt{\kappa \tau_p}$$

Where τ_p is the pulse duration, and κ is the thermal diffusivity constant of the material.

After understanding the laser-matter interaction mechanism, it will be easier to mention the laser ablation that can be considered in three main mechanisms: direct, indirect ablation, and both combinations.

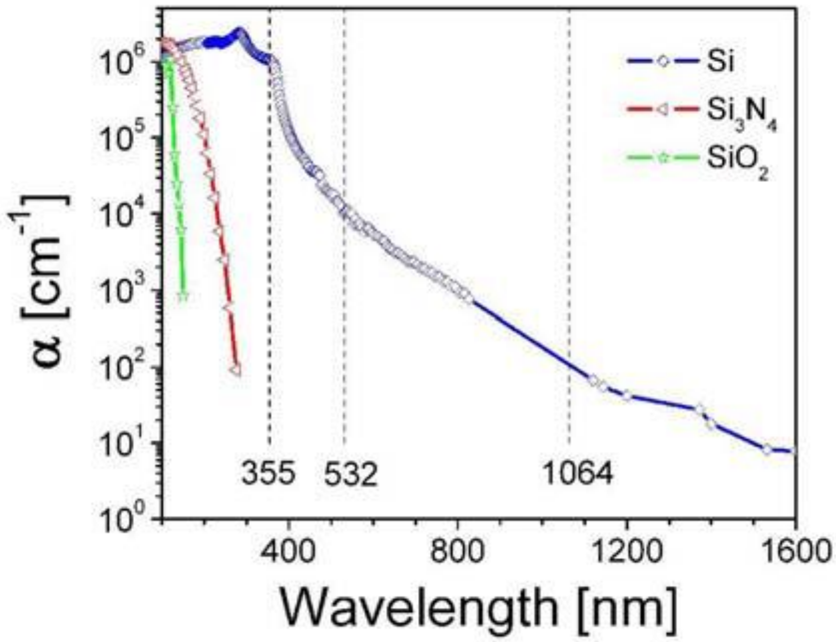

Figure 2.15 Absorption coefficient vs wavelength of 355, 532, and 1064nm for Si, Si_3N_4, and SiO_2 [40].

In the indirect laser ablation, the laser beam energy is restored in the Si substrate if the photon energy exceeds the silicon band gap energy but not the dielectric band gap energy. Moreover, the pulse duration of the laser beam is in the ns regime. [16]–[18]. The dielectric layer breaks down and lifts off from the surface by the high gaseous pressure and high mechanical stress due to the melting of the underlying c-Si layer. In direct laser ablation, the laser intensity is high and absorbed in the dielectric layer. This direct ablation is generally induced by ultra-short pulses with pulse duration of ps and fs. Also, the laser beam can affect the silicon and dielectric layer, and the share of energy occurs, so both direct and indirect ablation are obtained. [19]–[22]. Those are three different laser ablation mechanisms shown in Figure 2.26.

This study uses different lasers with 532nm 5-15ps laser and 1064nm ns laser as the effect of different lasers can be understood. The reason for selecting this type of laser is the implantation of plated contacts suitable for mass PV production lines. Since the indicated lasers already exist in the production lines for selective emitter formation, rear laser contact openings, and cutting purposes. Moreover, these 532nm and 1064nm lasers have relatively lower prices than the other 266nm and 355nm lasers. While depositing the plated contacts, extra equipment prices also reduce the attractiveness of the alternative method.

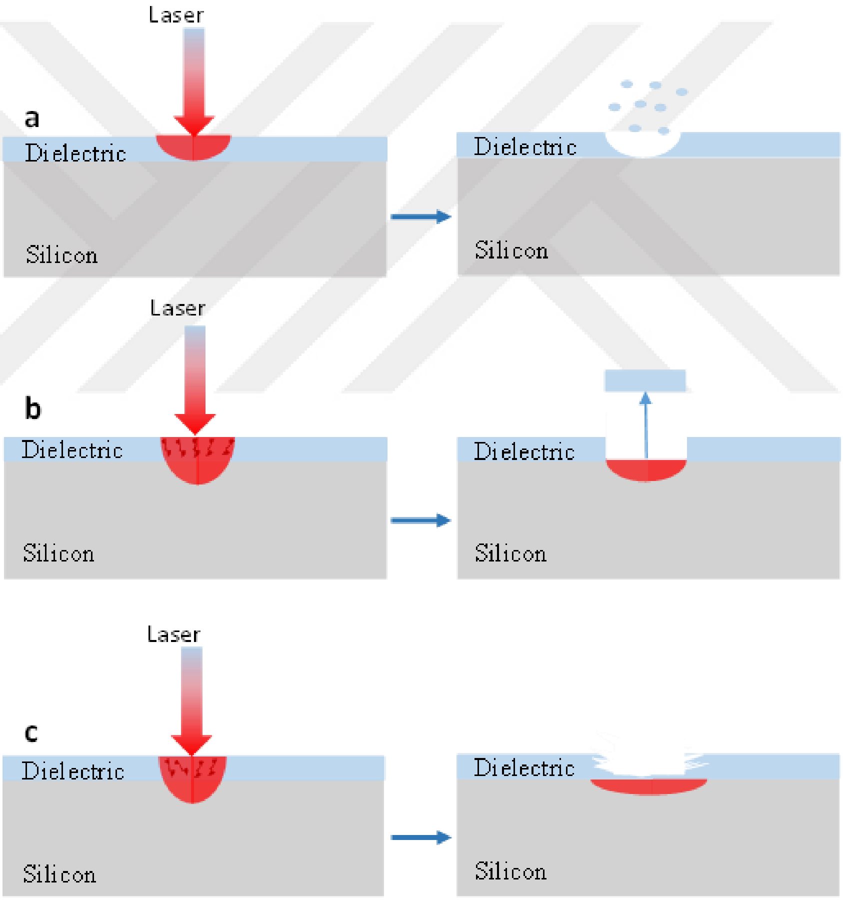

Figure 2.16 Laser absorption in a) the dielectric, b) the Si, and c) both the Si and dielectric [40].

Laser ablation of the SiN_x layer will be done with 532nm and 1064nm lasers. During the ablation, the underlying Si layer will absorb the laser light so that indirect laser ablation occurs. Therefore, the laser damage of the underlying layer and nonuniformities of the ablated areas will be investigated and minimized by the given laser parameters to have efficient solar cells.

Laser parameters play a crucial role in determining the quality of laser ablation and efficiency of the solar cell. Starting from the power of the laser, pulse duration, wavelength to repetition rate and their significant effects on the laser ablation are indicated as follows:

- Laser power with the unit of watts (W) is the transferred energy to the material that interacts. As the laser power increases, the risk of damage is also increased by the higher amount of heat transfers. Insufficient laser power causes the dielectric layer's non-ablation or nonuniform ablation.
- Laser pulse duration with the unit of ns, ps, or fs is the time passed during the energy transfer to the material. As the pulse duration decreases, the heat-affected zones are minimized, and the damage introduced by the laser is reduced.
- Laser wavelength with the nm unit plays a critical role in the light-matter interaction; as mentioned above, different laser wavelengths are absorbed in other regions. For example, 1064nm and 532nm lasers are absorbed in the Si rather than $SiN_{x.}$ However, the 355 and 266nm lasers are directly absorbed in the SiN_x. Therefore, the laser wavelength is critical during the modifications created in the surface or the underlying layers.
- The laser frequency of repetition rate with the units of Hertz (Hz) determines the time interval between laser pulses. As the laser frequency increases, the faster the pulses receive the material, the higher the processing speed.

The process of laser ablation plays a critical role in both plated contacts and the efficiency of solar cells. The optimization of laser parameters determines the contact patterns on the SiN_x passivation layer for following Ni/Cu/Ag plating. Laser parameters greatly impact obtaining a precise, uniform plated contact and less damaged removal of SiNx [23]–[25]. While the contact resistivity values and adhesion are determined by the Ni-Si phase formations, laser ablation of the dielectric layer specifies the location of Ni-Si formations by various patterns with complex effects. So, the laser parameters require careful optimization for improving the diffusion of Ni into the Si substrate by thermal energy transfer to the Si surface without creating pathways for unstable silicide formation. The laser energy transferred to the crystal structure of silicon during laser ablation can influence silicide formation by causing modifications to the crystal structure, inducing stress, and creating defects as the sample undergoes rapid heating and cooling.

Laser ablation's effects on forming Ni-Si phases can be combined with the annealing process. Therefore, to create a controllable and optimized silicidation of Ni with low contact resistance and good adhesion, heat treatment following the laser ablation and metal deposition plays a significant role in the optimized Ni-Si formation.

2.4.4.2 Contact Formation by heat treatment

Silicidation forms a silicide during the reaction between the silicon and a transition metal such as nickel, titanium, or cobalt during the fabrication of solar cells. Silicides' role is to improve electrical contact features in the interface of metal and silicon bases. In this study, Ni-Si phase formation by silicidation will be investigated. This Ni-Si phase formation improved the Ni/Cu/Ag metal contacts' electrical conductivity by elevated temperature subjection after the Ni deposition. In this process, Ni reacts with the Si base and forms a silicide to benefit the contact of solar cells. The first purpose of silicide formation is the reduce contact resistance to enhance the electron flow and improve solar cell performance. The second purpose is to improve metal adhesion by providing robust and hard-to-peel contacts between metal and silicon surfaces. The last purpose is to be a barrier for the deep diffusion into the silicon base to not short the cell, especially for the Cu diffusion.

The silicide formation process is affected by several parameters: temperature, time of annealing, and type of metal. The temperature of annealing affects the Ni-Si silicidation layer growth. Incomplete silicidation occurs at too low temperatures, and over diffusion with damaging the underlying Si layers occurs at too high temperatures. The reaction and forming of the silicide are examined by the annealing time. In the Ni seed layer plating context, Ni metal is chosen due to having high conductivity values for silicide formation. Each different metal determines its properties for the silicidation.

The temperature regime investigations will be done with TLM and SunsVoc. Furthermore, the dominant Ni-Si silicidation is presented in Figure 2.17 [26]. When the temperature is employed for contact formation, starting from 300℃ to 550℃, phase proportions with Ni or Si-rich phases are presented. As the temperature increases, Ni metal difuses into silicon, and phases contain more Si. At some temperature ranges, the lowest contact resistive Ni-Si phase having more stability is formed. This phase is the NiSi and preferred for the Ni seed layer formation for enhancement of lowest contact resistivity. With the light of temperature vs. phase proportion graph annealing temperatures are determined.

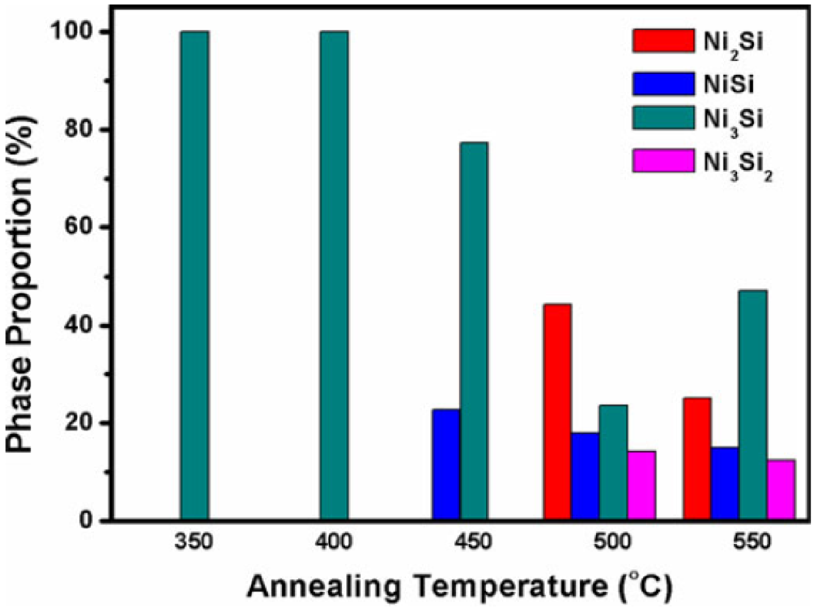

Figure 2.17 Annealing temperature vs phase proportions graph for Ni-Si phases [26].

CHAPTER 3

FABRICATION AND CHARACTERIZATION

3.1 Fabrication

This chapter explains the fabrication of PERC with front-plated Ni/Cu/Ag contacts, and experimental procedures for different purposes are indicated. Starting from the front side, SiN_x dielectric layer ablation, plating of each metal layer, and finally, the firing procedures are introduced with a detailed explanation. For the laser ablation part, laser parameters are determined for less damaged underlying layers with a 532nm ps laser and 1064nm nanosecond laser. Two separate laser ablations in laser-induced damages will be considered with various laser parameters. After locally ablating the front dielectric layer, the plating method performs front metallization on the opened areas. Plating rates, duration, and electrolyte quality are investigated for the plating part while depositing Ni, Cu, and Ag separately. Various temperature profiles were applied during the fast-firing part to form the low-resistive, adhesive, and long-term durable front contacts.

3.1.1 Laser Ablation

The laser ablation process is used for the front side contact openings to plate the front Ni/Cu/Ag metal stack. Laser ablation is one of the most used methods to open the dielectric layer and get the contact for the plating process due to its fast, contact-free, and precise alignment of the front grid pattern. However, laser ablation of the dielectric layer is crucial, which means non-optimized laser parameters can cause insufficient ablation of the dielectric layer, melting the underlying Si and forming amorphous silicon, sinking for Cu diffusion, microcracks, and defect centers [27]–[29]. Ablation mechanism, each laser parameter, and their impact are listed in detail.

.

In this study, laser ablation of the dielectric layer is performed by 1064nm ns and 532nm ps pulsed lasers to determine the ablation effect on the plated metal properties and cell efficiencies. Various laser parameters for both lasers are indicated in Table 3.1

Table 3-1 Laser types and parameters.

Laser Type	Parameters
1064nm ns laser	Power (0-100%) Frequency (30-80kHz) Draw-step(1-150LSB) Step Period(1-2000μs)
532nm ps laser	Power (0-100%) Frequency (200-1000kHz) Scanning speed (0.1-15m/s)

EO Technics-SuperMarker GF311 nanosecond IR laser with 1064nm wavelength and 30W max power is used for the SiNx dielectric removal. The power, frequency, and draw step ranges for the 1064nm ns laser will be scanned to see the effect on the surface modifications. IR 1064nm ns laser tool that has an optical lens unit, stage with vacuum and nitrogen gas, and control PC. The wafer is placed on the stage with a constant working distance of 325.1mm, and the vacuum pump is turned on to stabilize the sample. A relevant MIME interface is opened to start the operation, and the different designs can be drawn from the interface. Laser parameters are laser pulse frequency [30-80kHz], power [0-100%] that has a maximum power of 30W, laser scanner motor parameters of draw step [1-150LSB] and step period [1-2000μs] and shown in Table 3.1. The draw step is the separation when the laser is turned on, and the step period is the time unit of the draw step. After entering the suitable parameters into the software, laser operation is started. Nitrogen gas is turned on during the process since ablated SiN_x residuals should be removed from the sample surface. After the procedure, the N_2 gas and vacuum are turned off, and the sample is removed from the stage.

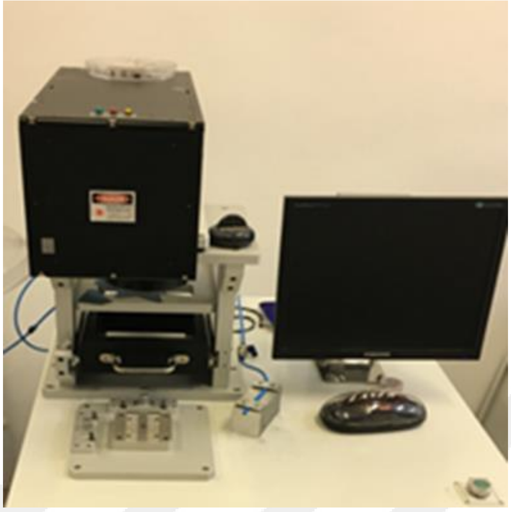

Figure 3.1 1064nm ns IR laser tool

Innolas Coherent HYPER RAPID 25 laser with a wavelength of 532nm, pulse repetition rate ranging from 200kHz to 1000kHz, and a pulse duration of less than 15ps laser is utilized for laser ablation of SiN_x layer. The laser's scanning speed [m/s] determines the distance between laser spots.

The various components of the laser system are the laser power supply, loading and unloading stages, control panel, and process chamber of the laser can be observed in Table 3.1. shows the 532nm ps laser parameters and their scanned ranges.

The control panel enables the use of Vision software, namely uVision A and uVision B, that monitors the wafer position on the stage throughout the process—the Human Machine Interface (HMI) software used for controlling the laser parameters outlined in Table 3.1. The Hyperapid program ensures the laser's operational status and connections. For creating the pattern of the contact openings, Iscribe software is employed by specific coded scripts [30].

In this study, parameter ranges for 1064nm ns and 532nm ps lasers are scanned for optimum laser ablation with less damage to the underlying layer and uniform deposition of plated contacts. Optimization results are given in section 4.1.

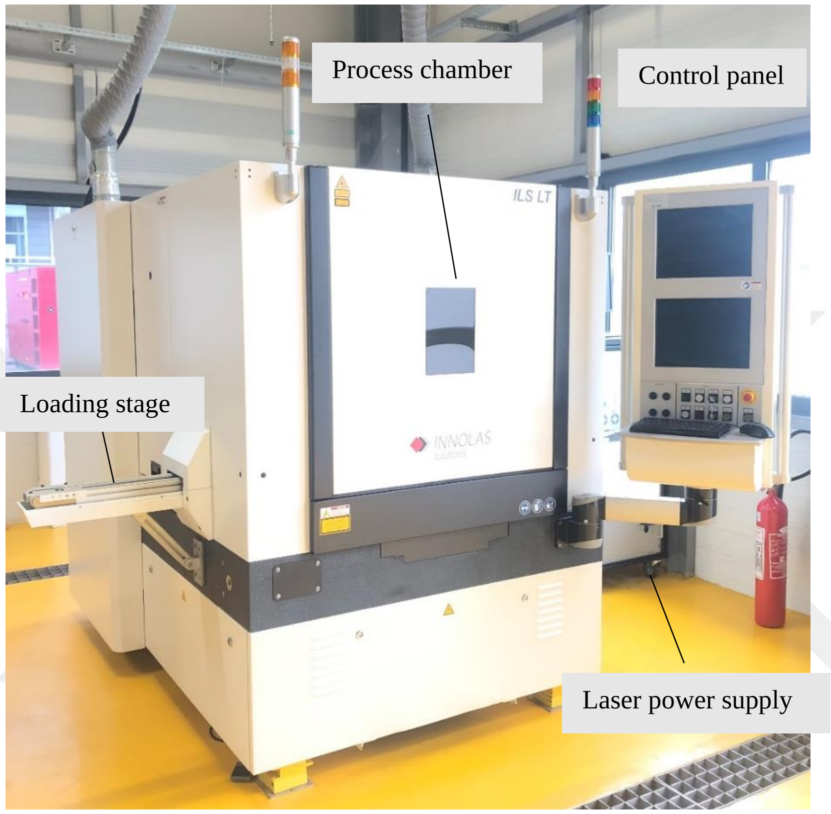

Figure 3.2 Innolas 532nm ps laser tool

A grid pattern is created for the samples, including several $2x2cm^2$ cells. Grid geometry is designed to give several different laser parameters on one wafer. The full-size wafer is required to operate the plating. After laser ablation occurs and grid design is obtained, the metal deposition rate is calculated.

The opened contact area is defined, and according to this area, the current density is given to the plating system. For example, for the 25 small cell grid design, the contact opened area is $30x10^{-5}$ dm finger width, 0.2dm finger length, and the number of 15 fingers, 7 fingers for BB are found as a total opened area of 0.033dm^2. The given current for 1A/dm^2 current density is 33mA.

Grid design is essential for the determination of current densities and laser parameters. There are three different grid geometries used in this study. First, one is designed to give several laser parameters on a single wafer to check the deposition quality. The second one was also designed for the same reason with the addition of TLM lines. The third one is also required to be able to measure the I-V curve for a specific measurement tool. Laser opening also determines the underlying layer damage since the number of fingers or thick busbar requires more laser pulse energy transferred to the silicon. That is the reason for choosing thin (including 4 or 5 lines) busbars for samples. Additional draws are also performed with laser for full-size metallization and stripe type (TLM measurements) and long BB, including stripes for I-V measurements (to get contact from the probe pins).

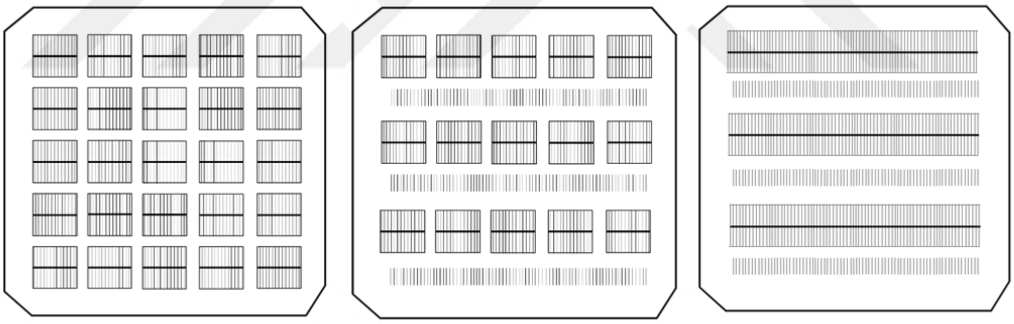

Figure 3.3 Grid design for little cell parameter scanning contact patterns

3.1.2 Metal Stack Deposition by Plating Method

There are three different plating setups for Ni, Cu, and Ag. Systems involve the same components, such as heating, pump, and light/ pH indicator switches on the front panel. Others are baths for the electrolyte of metal, connection cables, sample electrodes, lamp, and external power suppliers. Figure 3.3 and Figure 3.4 illustrate the process setups and tools for Ni, Cu, and Ag plating.

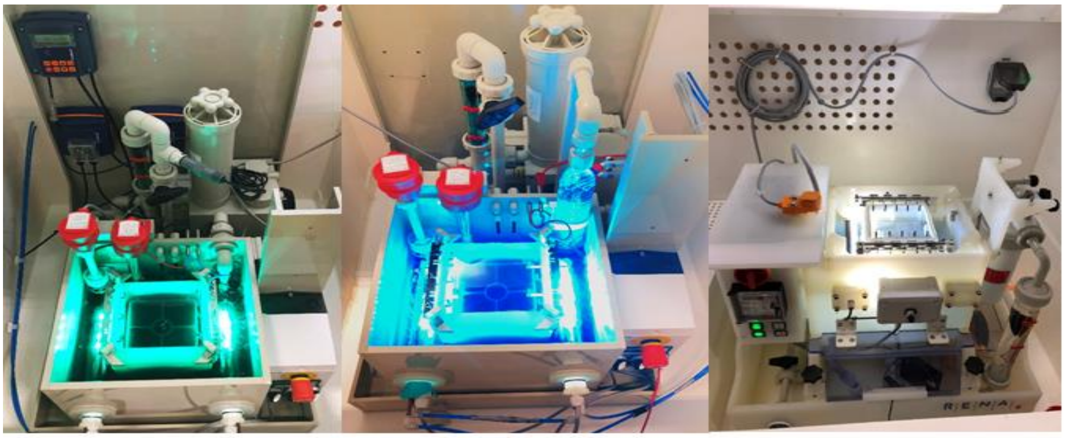

Figure 3.4 Plating tools from left to right for Ni, Cu, and Ag, respectively.

Temperature and pH must be optimum values for uniform and good-quality metal deposition before starting the process. The positive terminal of the external current/voltage source is connected to the electrolyte to separate metal ions and counter ions. The negative terminal is connected to the solar cell's rear surface to supply electrons by stabilizing metal ions to form a thin metal layer on the electrode. In the same way, electrodes are placed on the rear side of the wafer for external current that crosses over the cell and supplies electrons to the ionized metal in the solution and on the front side to create a pathway for metal deposition. After the solar cell placement and connection of cables on the sample holder part, the electrolyte is pumped through the sample's front side. The electrolyte for Ni is NB Semiplate 100, Cu is NB Semiplate Cu 100 purchased from the NB Technologies company, and the Ag electrolyte is the Macdermid HELİOFAB AG-340. Halogen lamps are turned on for light-induced metal plating by photo-generated current, and the power supply deposits the metal by giving external current to obtain more deposition rates. A stopwatch controls the time of deposition, and the connections of cables are checked with a multimeter. Finally, the deposit is made, and the solar cell is removed from the holder, rinsed with DI water, and dried with nitrogen gas for further plating processes. After each metal deposition, rinsing and drying procedure is required not to contaminate the bath solutions and to remove solution residues from the surface of the substrate.

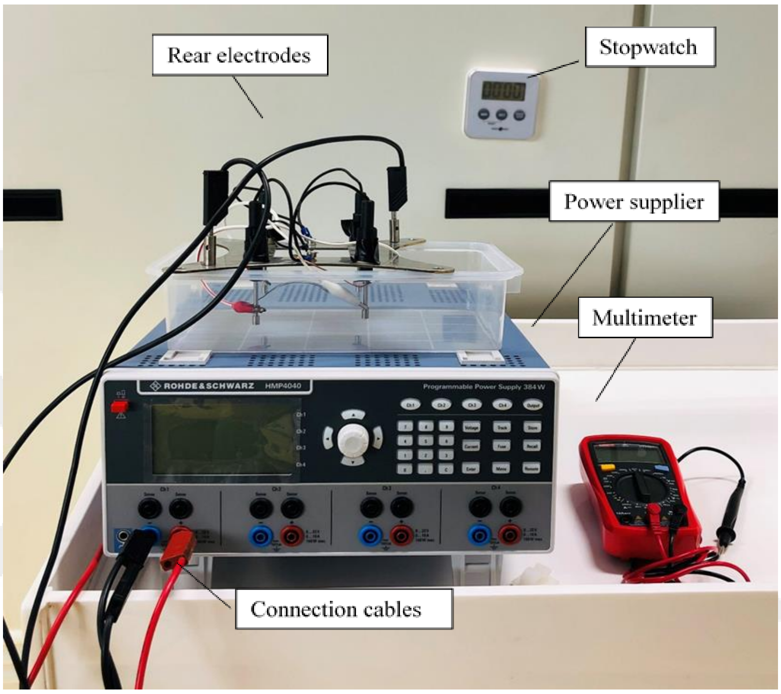

Figure 3.5 Stopwatch, power supply, multimeter, and back contact electrodes with connection cables for the plating process.

3.1.3 Nickel Seed Layer

Ni seed layer is plated on the ablated areas to eliminate the detrimental diffusion of Cu through the Si and improve the contact adhesion by forming nickel silicide phases. Ni seed layer is deposited by NB Tech. plating tool that contains NB Technologies Ni semi plate 100 electrolytes, LED, a pump, temperature controller, and pH controller. The bath temperature of the Ni electrolyte is set to 40°C, and the flow of the electrolyte is arranged as the solution interacts with the whole wafer's front surface for the pH of the electrolyte 3.25 is set by adding sulphumic acid which lowers the pH. For the LIP, the light is turned on. For the bias-assisted plating, the cables are connected to the cathode and anode parts of the setup, and the selected constant current values are given to determine the deposition rate. The unit used for the current density is classified from 1A/dm^2 to 8A/dm^2.

The purposes of variable input current densities are to obtain uniform height and width coverage of the Ni to the opened areas and to control the aspect ratio.

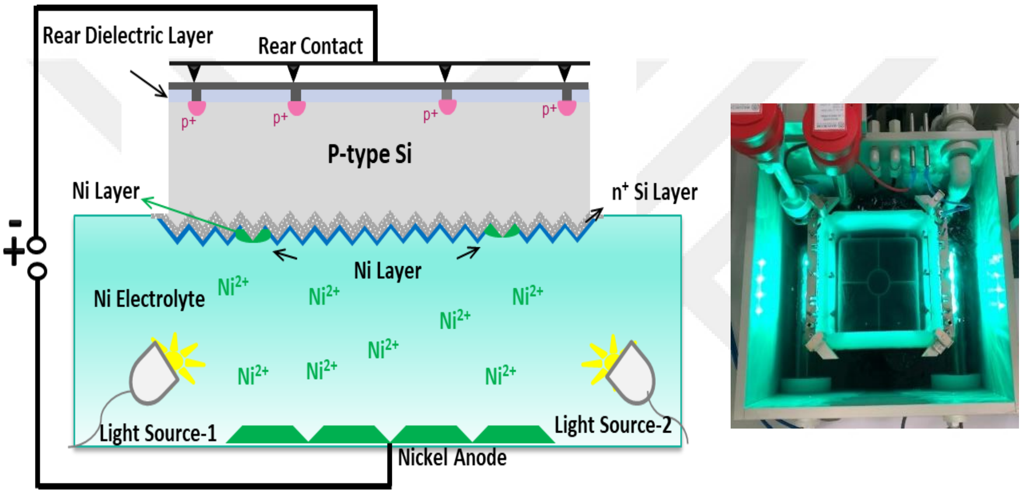

Figure 3.6 Schematic drawing (left) and picture (right) of Ni plating bath.

The components to make the 10 liters of Ni electrolyte and their purpose are given in Table 3.2

Table 3-2 Products used in Ni electrolytes are purchased from the NB technology.

Product	Purpose
NB semi plate Ni 100	To decrease stress and
Ni 100 anode activator	To improve conductivity
Ni 100 add. agent	To refine the grain and smooth the shiny surface
Nickel sulfamate solution	To make-up Ni
Boric acid	To prevent sudden changes in pH
Sulphamic acid	To lower the pH

In the Ni electrolyte, some reactions to deposit the metal on the surface are reduction reactions. The basic Ni ionization and stabilization formulas are given in the below such as:

13

$$Ni + 2H^{+} \rightarrow Ni^{2+} + 2[H]$$

14

$$Ni^{2+} + 2[H] \rightarrow Ni + 2H^{+}$$

Reaction (1) represents the anodic reduction of Ni in the electrolyte, and reaction (2) represents the deposition of Ni by taking an electron from the solar cell's front surface.

During the deposition of Ni, the current density given externally is differentiated between 1A/dm^2 to 8A/dm^2 to understand the relation of current density with contact adhesion, aspect ratio, and uniformity of contact width and height. Moreover, the deposition time of the Ni deposition process is varied between 1 min to 15 mins.

These ranges are specified with the literature considerations and availability for industrially feasible production [31]–[33].

3.1.4 Copper Conductive Layer

The copper electrolytes are copper sulfate, a brightening agent, brightening carrier, and unique acid copper plating formulations of semiplate Cu 100 and Cu 100 makeup. Thanks to these ingredients, flexible, ductile, low-stress, power-throwing plated copper metal is deposited on the Ni seed layer.

The same experimental procedure is applied to deposit the Cu conductive layer. pH, temperature, and pumping are arranged as the optimum deposition occurs. Again, externally, the current density is varied on the Ni seed layer to determine the width and height of the contacts about adhesion and uniformity. Surface morphology, width, and height of the contacts before and after Cu plating can be seen in the related results section.

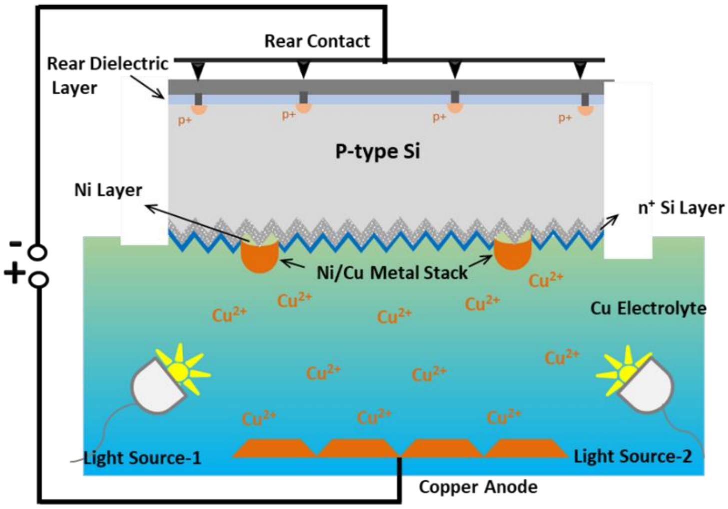

Figure 3.7 Schematic drawing of Cu plating.

3.1.5 Silver Capping Layer

There is a requirement for an Ag capping layer to prevent Cu oxidation. Also, to ensure durability and minimize the degradation of metal contacts. Ag is selected since it has the highest conductivity for interconnections of solar cells in the module integration step and is less resistant to oxidation reactions. Since the amount of Ag used as a thin 1-3nm capping layer is less, the cost of production is still lower than screen-printed Ag contacts.

The Ag electrolyte employed is the Heliofab Ag-340, which boasts uniform deposition, brightness, excellent conductivity, and ease of maintenance. This electrolyte is composed of silver and special formulations to ensure uniformity and stability in the metal content of Ag. It also contains additives to control cathode current density, potassium hydroxide to elevate pH, and methanesulfonic acid to reduce pH.

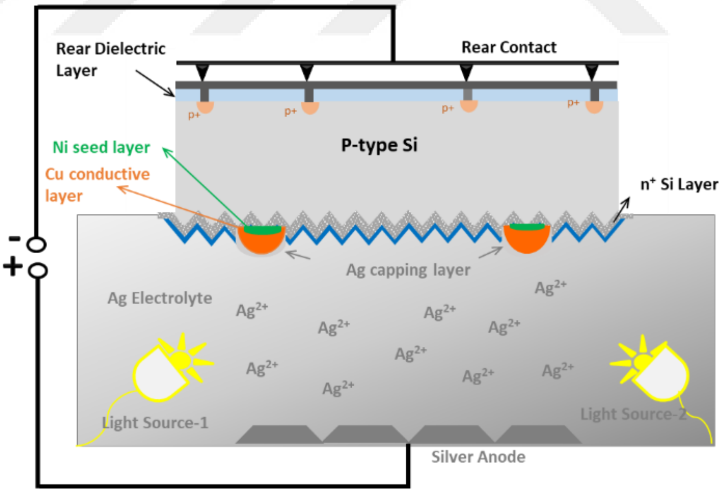

Figure 3.8 Schematically drawing and picture of Ag plating tool.

3.1.6 Annealing for Front Contact Formation

Plated contact formation performed by the annealing in the industrial belt furnace is suitable for mass production in a tube furnace with an N_2 atmosphere and a hot plate with an N_2 atmosphere. The belt speed and temperature are alternated to obtain the lowest contact resistance values. Temperature ranges between 200°C to 700°C. The belt speed of the fast-firing oven affects the time duration of a given temperature and varies between 100 to 500cmpm, roughly corresponding to 1-5 minutes. For the tube furnace, temperature ranges between 200°C to 700°C again, with 1-10 minutes duration. As a last method, a hot plate is used by the N_2 present to get rid of the oxidation of metal contacts. Temperature is ranged between 200°C to 500°C with 1-10 minutes duration time. Experiment sets can also be observed in Table 3.1. The contact resistivity values depend on the formed Ni-Si phases with a range of temperatures in the literature [34]–[36].

Table 3-3 Annealing tool and scanned parameter ranges.

Annealing Tool	**Scanned temperature range and durations**
Tube Furnace	200-700 / 1-10 minutes
Belt Furnace	200-700 / 1-5 minutes
Hot Plate	200-500 / 1-10 minutes

Figure 3.9 Industrial SinTerr fast-firing oven tool.

Figure 3.10 Annealing furnace with N2 gas atmosphere.

3.2 Characterization

3.2.1 Electrical Characterization

In this section, electrical characterization methods, which are SunsV$_{OC}$, I-V curve measurement, Dark IV, and TLM, will be presented, and their usage purpose will be expressly indicated.

3.2.1.1 SunsV$_{OC}$

SunsV$_{OC}$ instrument is used to identify the electrical performance of the solar cells based on the V$_{OC}$ by eliminating the series of resistive losses developed by Sinton et al. The measurement tool is Sinton WCT-120 [37].

Figure 3.11 Sinton SunsVoc tool.

The components of the system are a flash lamp, a digital oscilloscope, a photodetector, and a computer. A solar cell is placed as the probe pin manually takes the front side contact, and the back side lies on the chunk. Then, illuminated by a flash lamp irradiating in a fraction of a second, V_{OC} is measured simultaneously. A digital oscilloscope has two channels: light intensity time dependence measurement by a photodetector concerning the reference cell and direct Voc measurement of the solar cell under the open circuit condition. So, pFF can be derived from the pseudo current density J vs. V_{OC} curve, and the difference between the FF and pFF comes from the R_{series} losses. Using the Sinton program, from the J_{dark}-V_{OC} and J_{light} V_{OC} curves, the effective lifetime of charge carriers, pFF, recombination of charge carriers, shunting, and η can be extracted.

3.2.1.2 I-V Curve Measurement

QuickSun 120CA-XL flash solar simulator at AM 1.5G I-V tool measures the I-V curve of little cells with full area. Additionally, series resistance (R_{series}), shunt resistance (R_{shunt}), fill factor (FF), open circuit voltage (V_{OC}), and short circuit current (I_{SC}) can be extracted from the IV curve. The I-V tool can be observed in Fig 3.11.

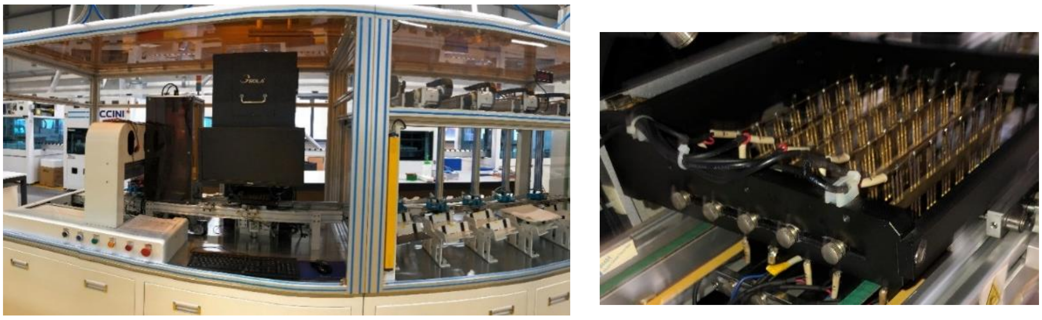

Figure 3.12 QuickSun 120CA-XL flash solar simulator tool.

3.2.1.3 TLM

The transfer length method (TLM) identifies three parameters of emitter sheet resistance (R_{sheet}), contact resistance (R_C), and contact resistivity (ρ_C). In classic TLM test structures, parallel fingers with the same width of 10mm (W) and different spacings (L_1, L_2, etc.) on the conductive layer are cut as a stripe by laser. Assuming that the sheet resistance value is constant over the sample with an equal contact resistance for each finger. It is possible to calculate resistances between one finger to neighboring fingers formulated as follows:

15

$$R_{1.2} = 2 \times R_C + R_{sheet} \cdot \frac{L_1}{W}$$

That gives the plot of spacing between fingers and resistances. By analyzing the plot shown in Figure 3.13, values can be extracted, including R_{sheet}, from the slope of the linear fit, R_C half of the R_{Total}value at the y-intercept, and transfer length (L_T,) from extrapolated x-intercept. By using Newton's method, the R_C and L_T can be formulated as:

16

$$R_C = \frac{\rho_C}{W L_T} coth \frac{W}{L_T}$$

17

$$L_T = \sqrt{\frac{\rho_C}{R_{sheet}}}$$

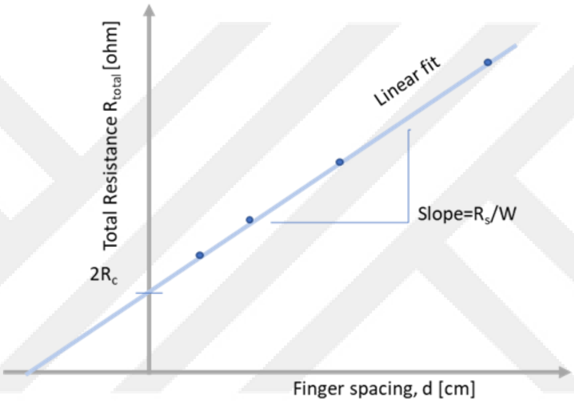

Figure 3.13 R vs. d plotted graph from the TLM measurement.

If the distance between the number of n fingers is constant L, the resistance between two fingers is:

18

$$R = 2R_C + (n+1)R_{sheet}\frac{L}{W} + nR_{sheet}\frac{d_{eff}}{W} = 2R_C + \frac{R_{sheet}}{W}\left[(n+1)L + nd_{eff}\right]$$

19

$$d_{eff} = 2L_T . tanh \frac{W_F}{2L_T}$$

d_{eff} is the effective width of intermediate fingers, W_F is the finger width over a length. Series contribution of the contact resistance $R_{S,cont}$ is:

20

$$R_{S,cont} = \rho_C \frac{d}{W}$$

d is finger spacing, W is finger width.

For the TLM measurement, finished solar cells are cut by laser as the finger stripes of W=7-10mm without finger connection such as a busbar. Stripes are placed on the relevant chuck with a vacuum, and the contact resistivity probe head is set from the joystick or given x and y coordinates on the fingers, and measurement is started from the software.

Figure 3.14 TLM tool.

3.2.2 Optical Characterization

3.2.2.1 Optical Microscope

Optical or light microscopes magnify surfaces by sending a focused beam on the sample surface and detecting the reflected light in the visible range. The essential components of an optical microscope are the eyepiece, objective lens, and CCD camera. Light is sent and passed through the objective lens to focus the beam on the sample surface. Light is reflected from the sample surface and captured by the eyepiece or CCD camera. Hence, detecting the reflected light produces a micrograph image on the eyepiece or PC monitor.

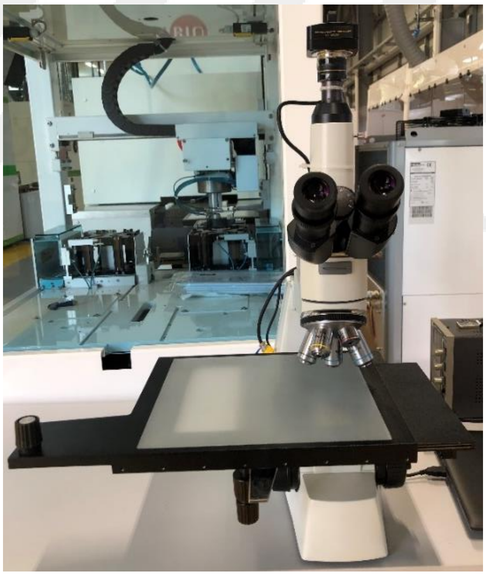

Figure 3.15 Optical microscope.

In this study, the optical microscope is used to analyze the solar cell surface after the laser ablation and metal depositions if the resolution range of the optical microscope is enough to observe the surface morphology.

3.2.2.2 Scanning Electron Microscope (SEM)

Scanning electron microscope has a resolution of up to 1nm by scanning the sample surface with a focused electron beam to give information about the composition and topology of the sample surface. An electron gun directs a beam of electrons on the sample. Those electrons are divided into two groups: back-scattered electrons with higher energies and secondary electrons with lower energies. Back-scattered electrons result from the elastic interactions of electrons with surface atoms that give compositional information while going further in the sample. Secondary electrons are inelastically reflected from the near-surface, so lower energies than back-scattered electrons provide topological information.Those two different electron groups from the specimens are detected separately and produce signals to observe the high resolution of the surface image on the PC monitor. A schematic representation of the SEM device and components are shown in Figure 3.16.

In this study, SEM images are used to observe the morphology of the ablated contact openings to understand the laser effect on the surface and width of plated metal contacts.

CHAPTER 4

RESULTS AND DISCUSSION

4.1 Laser Ablation of Dielectric Layer

The laser ablation process involves using two industrial lasers with 532nm (ps) and 1064nm (ns) wavelengths. The main reason for employing those specific lasers is to integrate the ablation process into existing PERC fabrication without the extra including of different laser tools. Specifically, the 532nm ps laser is primarily utilized for rear local contact opening, and the 1064nm ns laser is for cutting and edge isolation.

The results are observed through SEM and optical microscopy images, focusing mainly on the surface modifications. Various parameters were examined, although a narrowing down of the scanning range is presented here. Table 2.3 indicates that all parameters are determined from minimum to maximum values for different laser scanning ranges and combinations.

Firstly, laser parameter effects are examined from separate SEM images. A 532nm ps laser ablation images will be displayed for the initial phase. This study's second part addresses how 1064nm ns laser ablation impacts the dielectric surface. After thoroughly evaluating surface morphology, optimum laser parameters are determined. Samples are ablated with selected parameters, followed by metal deposition to see the laser influence on the plated Ni/Cu/Ag front metal stack.

Figure 4.1 shows the laser frequency range from 200kHz to 1000kHz. Frequency determines the time that passes during the laser pulse absorption by the material. While frequency ranges, other parameters such as scan speed of 0.1m/s and power percentage of %100 are kept constant. The reason for high power and low scan speed is to observe the laser frequency effect on the surface more clearly.

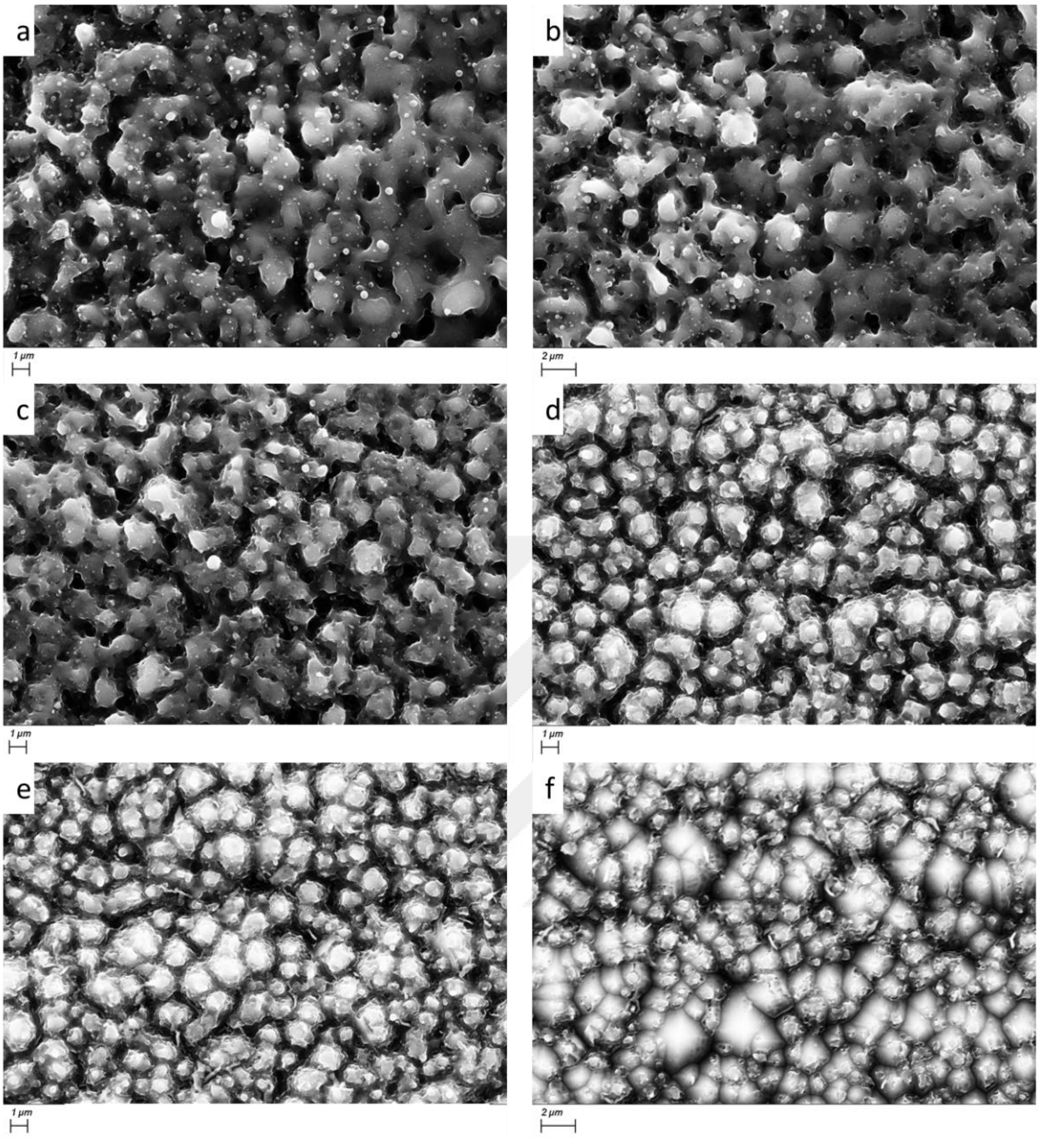

Figure 4.1 SEM images of laser ablation with frequency of a) 200kHZ, b) 312kHz, c) 400kHz, d) 600kHz, e) 800kHz, and f) 1000kHz.

The ablation process starts with laser pulse energy absorption on the underlying c-Si since the SiN_x layer behaves transparently for the 532nm laser. In this 532nm laser ablation, the c-Si is disordered, and a thin a-Si can be formed if the laser energy is insufficient. As the laser energy is increased and high enough to melt c-Si, SiN_x expands and breaks down due to high mechanical stress. Thus, the removal of the dielectric layer is obtained [21].

In Figure 4.1, as the laser frequency increases from a) 200kHz to f) 1000kHz, the surface's damage is less, which means the fluence of the laser is getting smaller and less melting of the surface is seen. In the SEM images, the melting of the surface is more detectable on the low-frequency values of 200, 312, and 400kHz. Increasing the frequency value up to 1000kHz, less surface melting is detected. Therefore, for less damage and melting of the surface, a maximum value of 1000kHz is selected.

Secondly, the laser power effect on the surface is observed in Figure 4.2. As the laser power increases, more energy is transferred to the matter, resulting in more surface damage. In Figure 4.2, the power of a) %50, b) %70, and c) %100 is applied to the wafer surface while other parameters, such as frequency and scan speed, are kept constant. Figure 4.2 c) %100 power has the biggest sign of melting and damage to the surface. As the power decreases to a) %50, there is less melting with opened dielectric areas. This %50 power value is the minimum value for removing the dielectric layer with a selected maximum 1000kHz frequency and a minimum scan speed of 0.1m/s.

Thirdly, laser scan speed plays a vital role in ablation, and as the scan speed increases, the laser-matter interaction takes less time, and the damage decreases. This impact can be seen in Figure 4.3, as the scan speed increases from a)0.1m/s, b)10m/s to c)15m/s less damage is observed. However, several combinations are done to determine scan speed to obtain less damaged laser ablation. While the increasing scan speed gives the narrow contact opening with less removal, the power value should also be increased. The power value is the most effective so that the laser scan speed is arranged with optimum frequency and power values. The balance of the three parameters’ combination is formed.

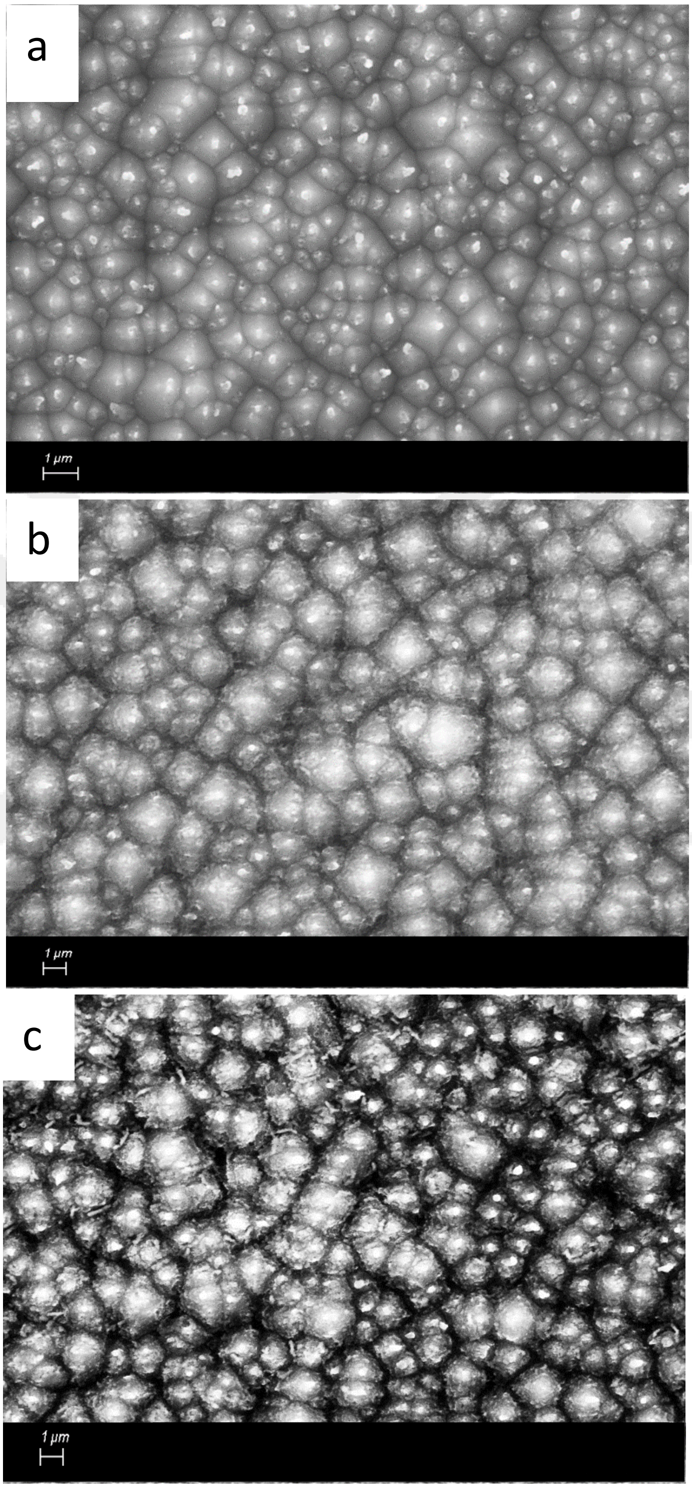

Figure 4.2 Laser power increases from a)50%, b)70% to c)100%.

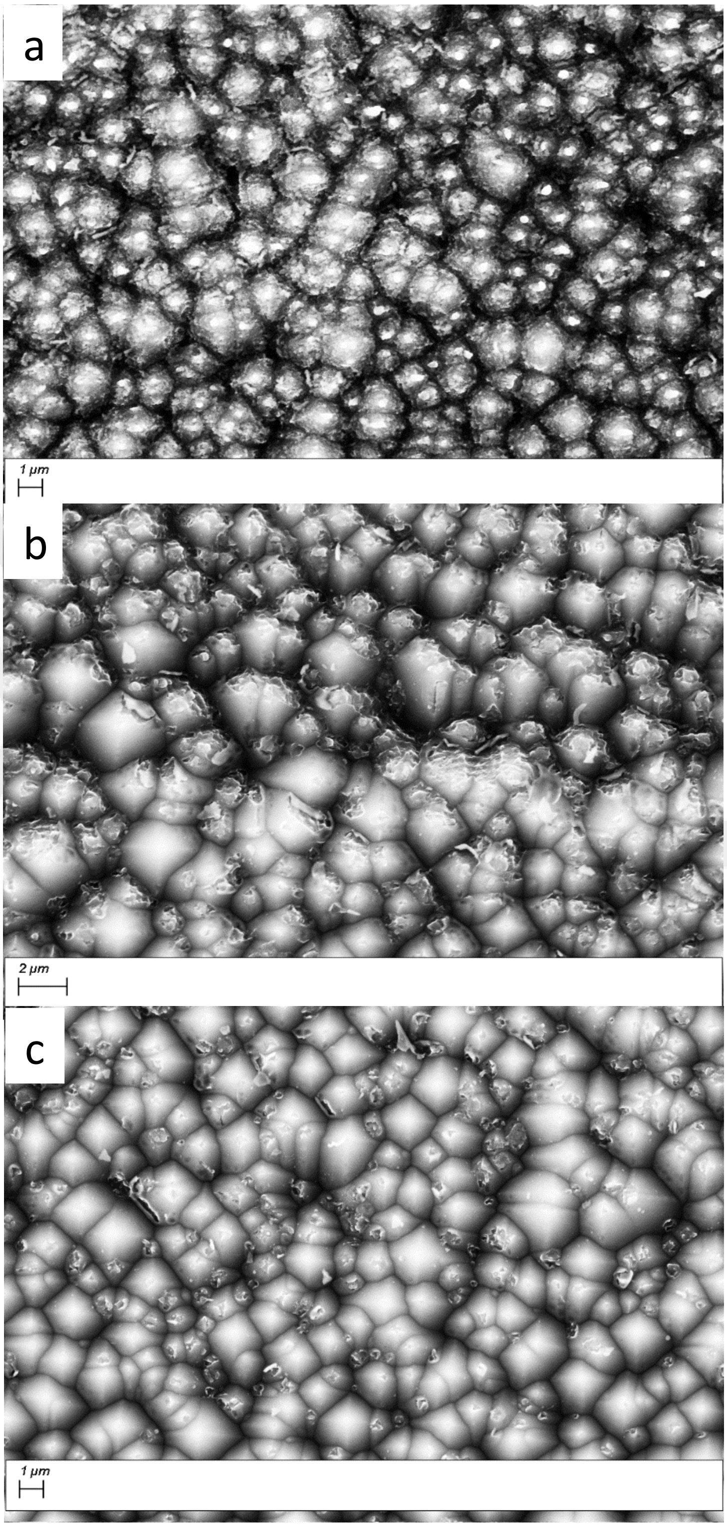

Figure 4.3 Laser scan speed increases from a)0.1m/s, b)10m/s to c)15m/s.

Therefore, SEM images revealed that the purpose of a less damage-free surface could be obtained by optimum parameters of power of 50%, frequency of 1000kHz, and a scan speed of 1m/s for the laser ablation with a 532nm ps laser. For this optimum laser ablation, SEM images are presented in Figure 4.4.

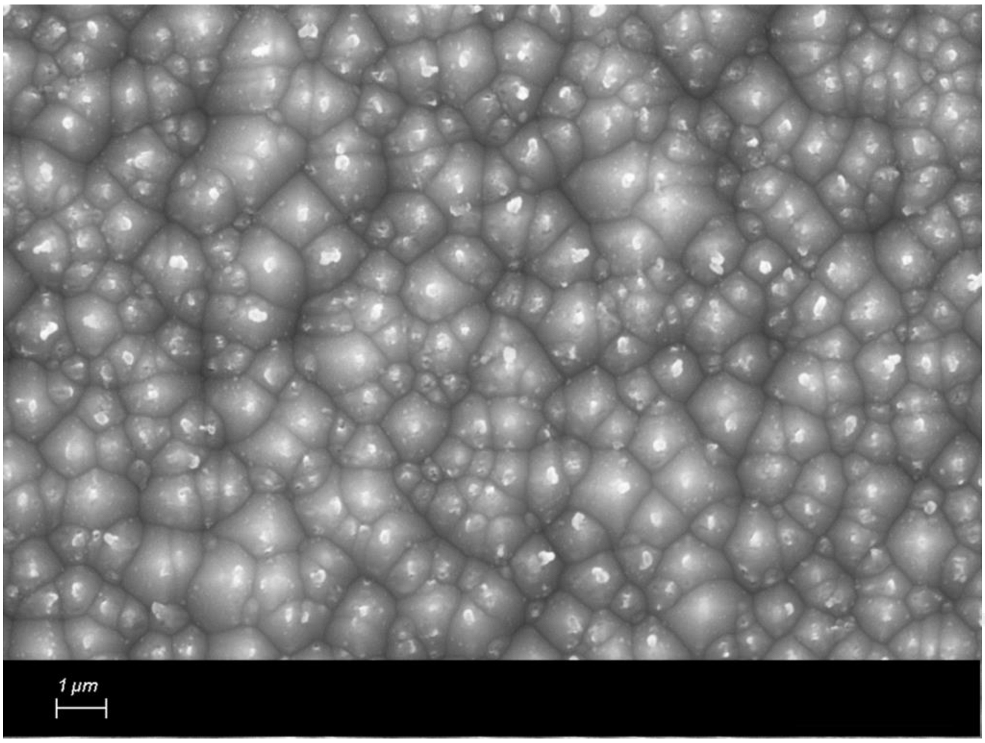

Figure 4.4 SEM image for 532nm ps laser ablation with 50% power, 1000kHz frequency, and 1m/s scan speed.

In the second section, ablation is performed by the 1064nm ns laser. The parameters of the 1064nm laser are laser current (or power), frequency, and draw step (or overlapping). SEM and optical microscope images indicate the effects of those parameters on the surface.

The first 1064nm ns laser parameter is laser current (%) or power (W). As the power increases, surface damage grows, just like the 532nm ps laser. Since the laser energy transfer is affected by laser power, more damage is introduced to the surface as the power increases. In Figure 4.5, the laser current increase from 25% to 100% can be seen with more melting of the surface at the constant overlap and frequency.

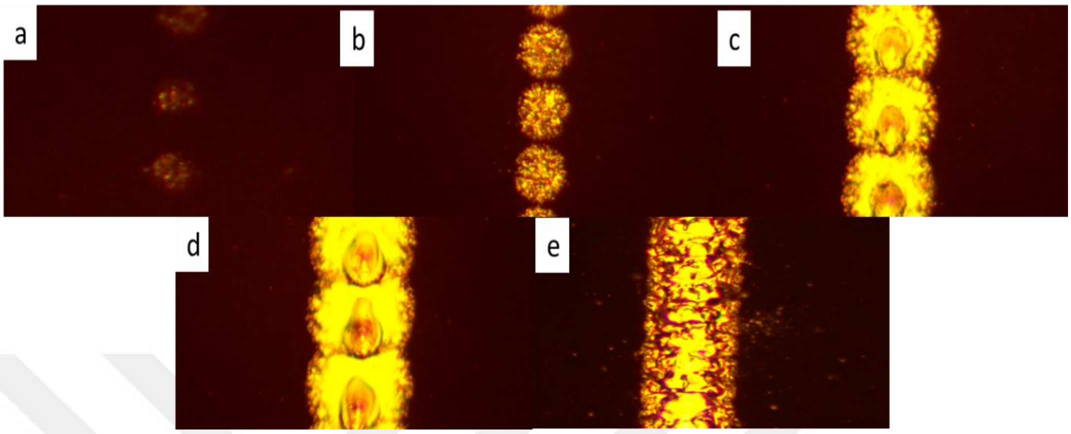

Figure 4.5 Optical microscope images of 1064nm laser ablation on the dielectric layer with the frequency of 80kHz, draw step of 65LSB, and current of a) 25%, b) 30%, c) 40%, d) 50%, and e) 100%.

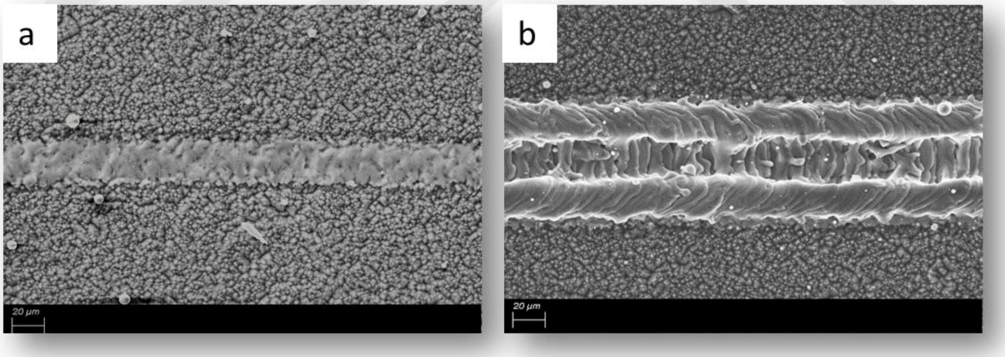

Figure 4.6 SEM images of power a) 50% and b) 100%.

Second, the frequency change also significantly affects surface modification; a higher frequency leaves less damage, and a lower has more impact. In Figure 4.6, optical microscope images explain this impact as the center of spots is more visible due to the Gaussian beam profile. As the frequency increases, less melting and detectable spot centers are shown in Figure 4.7 c). So, the maximum frequency of 80kHz is selected for laser ablation of the dielectric layer.

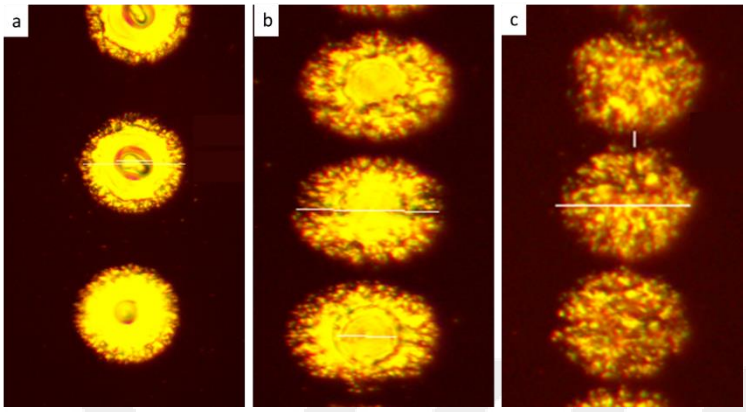

Figure 4.7 Optical microscope images of 1064nm ns laser ablation on the dielectric layer with 30% current, 65LSB draw step, and a) 30KHz, b) 50kHz, and c) 80kHz.

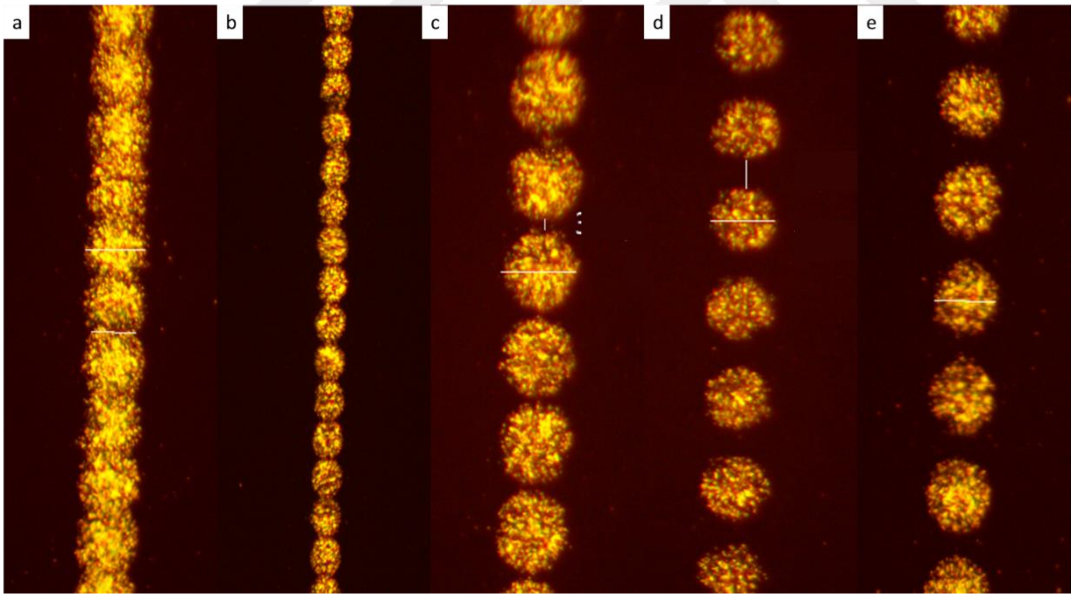

Figure 4.8 Optical microscope images of 1064nm ns laser ablation on the dielectric layer with 30%power, 80kHz frequency, and a) 45LSB, b) 50LSB, c) 65LSB, d) 70LSB, and e) 75LSB.

The drawing step is the third and final parameter of the 1064nm ns laser, which dictates the degree of overlap between laser spots. As the drawing step decreases, the spots overlap more, resulting in an increased width of the exposed contact area. Limiting the number of times the laser spots open on the surface is crucial to minimize damage. Therefore, in the same region, only one spot should be opened to reduce the risk of laser damage and shunting probability.

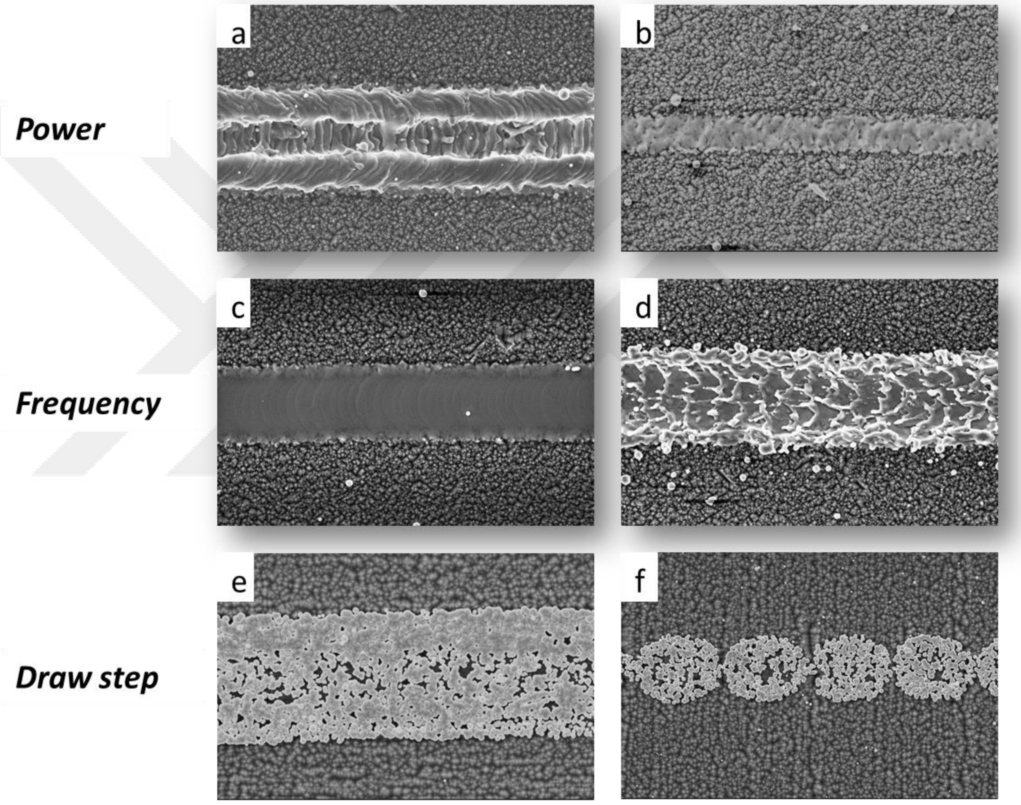

Figure 4.9 SEM images of 1064nm ns laser power of a) 70% and b) 50%, frequency of c) 80kHz and d) 30kHZ, draw step of e) 10LSB and f) 50LSB%,

The finding offers implications for 1064nm ns laser ablation parameters that determine the surface morphology with alternating features. Laser power percentage of 30, frequency of 80kHz, and draw step of 65LSB are investigated as the optimum laser ablation parameters before the Ni seed layer deposition by plating. In the context of identification, many combinations were experimented with. However, testing all possible combinations is a challenging task. Ultimately, the 1064nm ns laser parameters were selected based on evaluating surface modifications and deposition quality. Once the optimal parameters were determined, SEM images were captured to evaluate the results, as illustrated in Figure 4.10.

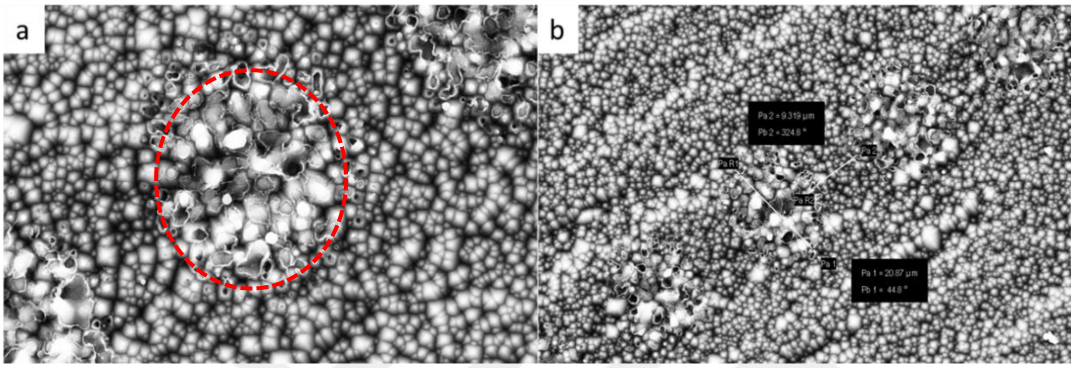

Figure 4.10 SEM images of dielectric layer ablation with 1064nm laser, 30% power, 80kHz frequency, and 65LSB draw step.

In the beginning section of the experimental results, the investigation of surface morphology revealed the optimal laser parameters for the 532nm ps laser and the 1064nm ns lasers. With these identified optimal laser parameters, the subsequent steps involving metal deposition for the Ni seed layer and subsequent characterization will be carried out in sections 4.2, 4.3, 4.4, and 4.5.

4.2 Ni Seed Layer Investigations

After laser ablation is implied for contact openings, the Ni seed layer is deposited on the laser-exposed patterned areas. The main deposition parameters are external current density, light exposure, and time. The current density range is scanned between 1A/dm^2 to 8A/dm^2 to understand the current density relation with contact adhesion, uniformity, and contact aspect ratio. Some experiments were done with light, and some were not to understand the light effect. When the light is induced into the plating system, uniformity increases due to the supply of photogenerated electrons through the open contact areas. Also, the ghost plating that is the unwanted plating outside the opened areas, became more detectable.

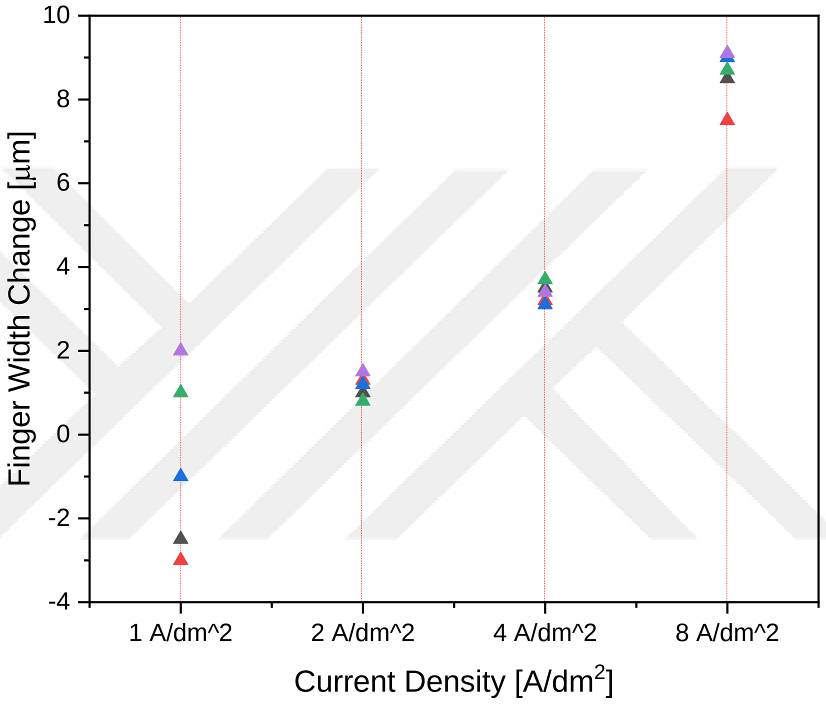

Figure 4.11 Graph of nickel current density vs. finger width change.

The optical microscope determines the contact width after the light-induced bias-assisted plating with various current densities. The contact width change for the opened areas is plotted as shown in Figure 4.11. This graph shows that with the current density of 1A/dm^2, the electrons are not uniformly transferred through the front surface contact openings. As a result, the Ni deposition is nonuniform. Moreover, in some parts, the contact opening width is higher than the deposited metal width, so the deposition is insufficient to fill the conductive laser opened pattern. Another result is the expansion is getting more significant by increasing the current density higher than 2 A/dm^2. The aspect ratio, the height-width ratio, is getting smaller by higher width between the 4A/dm^2 to 8 A/dm^2. Therefore, the optimum current density for minimum width and uniform deposition is 2A/dm^2.

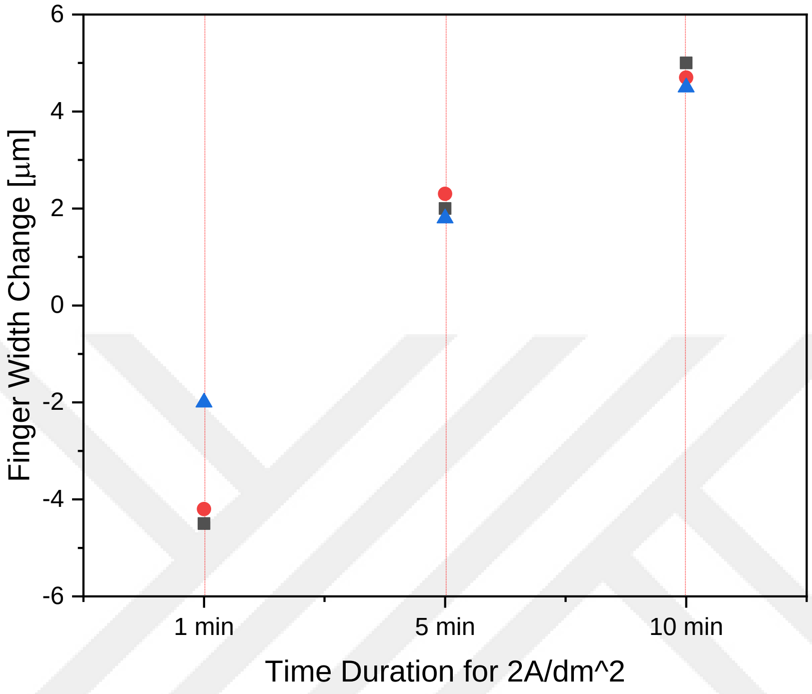

Figure 4.12 Finger width change vs. time duration of Ni deposition.

In Figure 2.12, similar uniform deposition is also determined by the time duration of deposition, and the time is varied between 1 to 10 min. The finger width change vs. duration time graph shows that the uniform and precise finger widths of the Ni seed layer optimized as 5 minutes of deposition time.

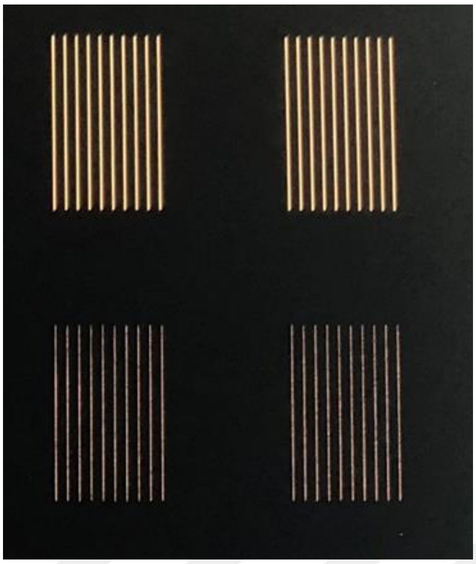

Figure 4.13 Uniformity comparison after Ni plating for $2A/dm^2$ - 5min (upper) and $1A/dm^2$ – 5min (lower).

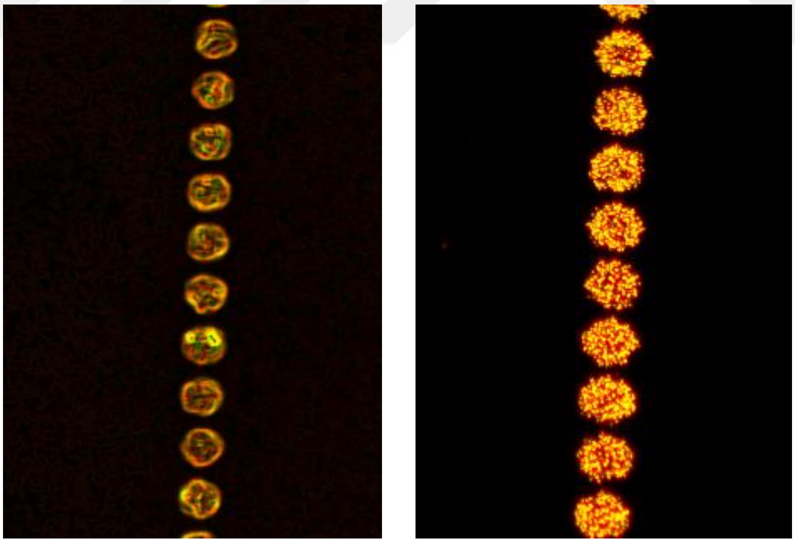

Figure 4.14 Optical microscope images of ablated spot size before Ni with an opening width of 23±1µm(left), after Ni with a width of 24±1 µm (right).

On the other hand, after annealing, the different current densities implied samples at the same temperature and time duration. In Figure 4.13, TLM results also assist the optimum current density and time duration of 4A/dm^2 value by having the lowest contact resistivity after Ni/Cu/Ag plating. However, it should be emphasized that the TLM results not only depend on contact uniformity and aspect ratio but have been impacted significantly by the temperature and time of annealing. TLM measurements will also be shown to investigate the Ni_xSi_x formation since Ni_xSi_x phases have different contact resistivity values. By annealing the Ni/Cu/Ag plated PERC samples, the lowest contact resistivity will be obtained by the NiSi phase, as indicated by the literature. These TLM results are presented in Section 4.5: Annealing for contact formation.

4.3 Cu Conductive Layer Investigations

Cu is the central part of the Ni/Cu/Ag metal stack and is classified as the conductive layer. After the uniform deposition of Ni, Cu is deposited on top of the Ni seed layer by the light-induced-bias-assisted plating method. Similar to nickel seed layer optimum current density investigations, Cu is also determined for its optimum current density and time of plating. Due to the exact reason for the aspect ratio, Cu needs to be deposited as high and narrow to have a high aspect ratio. The optimum current density is 4A/dm^{2,} which is investigated by the optical microscope width measurements. In Figure 4.12, the Cu-plated contact on the Ni seed layer with the 4A/dm^2 current density and deposition time of 10 min can be seen. The spot distances after the Ni deposition were still observable; however, the Cu plating connects spots. Due to its nodule structure, it contributes to a decrease in shading for the front side. Therefore, the Cu is deposited and needs a capping layer to not oxidize during the annealing and long-term oxygen reactions.

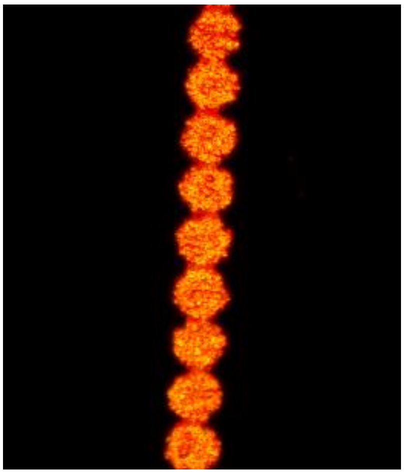

Figure 4.15 Optical microscope images after the Cu plated by Bias-assisted LIP on the Ni seed layer.

4.4 Ag Capping Layer Investigations

Ag is needed to cap the Cu conductive layer and only light-induced to plate the Ag. The reason for not assisting the plating with external bias is that the Ag capping layer does not have to be thick and is enough to cover the Cu layer with a height of 1-2um. Only light-induced plating is also preferred for Ag because the Ag electrolyte has a transparent appearance, and light beams can transfer through the electrolyte to reach the wafer front surface more easily than the Ni and Cu electrolytes. Ni and Cu electrolytes are less transparent to light than Ag electrolytes, which supports a higher deposition rate when only light-induced plating is performed for Ag capping laser deposition. So, the only variable parameter is the time of light exposure for Ag deposition, which is varied, and it is found that 3 minutes is enough to cover the Cu layer.

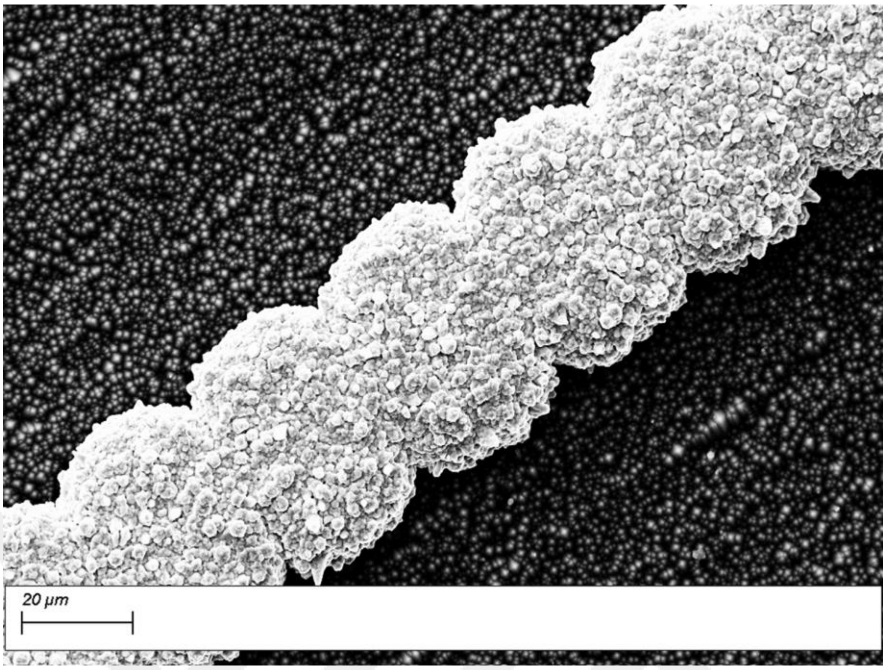

Figure 4.16 SEM image after plated Ag capping layer.

4.5 Annealing Temperatures Investigations

Tlm tool is used to examine the contact resistivity after the formation of Ni/Cu/Ag front stack. Contact resistivity values change with temperature and time duration of annealing. During the measurements, our tool gives pin check failed error due to the thin Ni barrier layer by itself. The probe must properly contact the metal pads during the TLM measurements to accurately measure contact resistivity on a textured wafer with pyramid structures. If the Ni deposition thickness is less than 5µm, the measurements could have errors since the probe could not properly contact the metal pads and would give erroneous values. The TLM results for different current density plated samples annealed, and the range can be seen in Figure 4.16. To solve it, additional layers of Cu and Ag are deposited, aiming to rectify errors in TLM results arising from the inability to measure thin nickel layers accurately. So, the annealing effect on the Ni-Si phase formation can be understood from the TLM results with the same Cu and Ag deposition properties to compare. Therefore, to investigate the NiSi formation, TLM is used to measure the contact resistivity of the plated Ni/Cu/Ag metal stack.

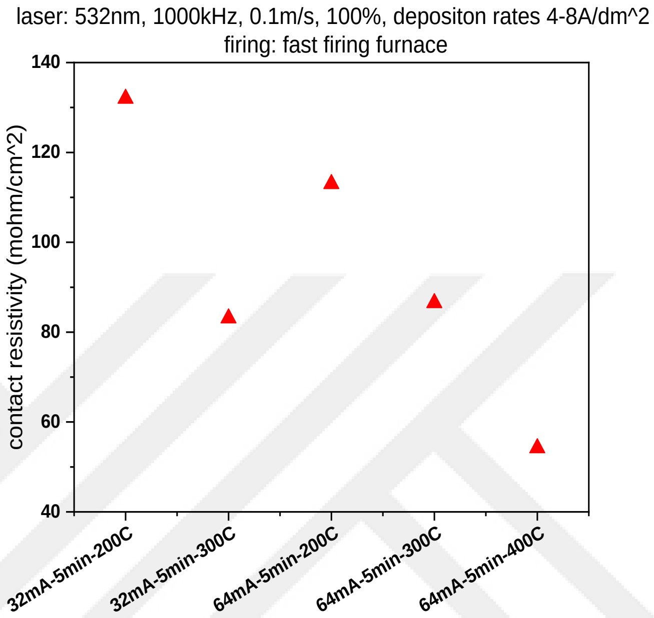

Figure 4.17 TLM results of contact resistivity values for 32mA-5min and 64mA-5min only Ni plated contacts at 200,300, and 400C.

As known from the literature, the lowest contact resistivity values are obtained in the specific form of NiSi that can give lower than 5mohm/cm [37].

As the temperature increases, shunting occurs since the metal diffuses through the n^+ doped Layer to the p-Si Layer. However, low temperatures will not be able to form the contact by forming a specific low-contact resistive Ni-Si interlayer. The temperature range must be carefully selected since the Ni-Si phases depend on the annealing temperatures. For example, the Ni_2Si phase occurs between 200-300°C, followed by the NiSi phase that can be observed up to 600°C. Subsequently, with an increase in temperature to around 700-800°C, the $NiSi_2$ phase forms[38], [39]. The temperature range for annealing is selected with the light of this information, and the time interval is scanned for different annealing methods of tube furnace, belt furnace, and hot plates. The range for annealing is indicated in Table 3.3, so the TLM results for this range are obtained. In Figure 4.17, the contact resistivity values vs. temperature time are displayed. The trend for lowering the contact resistivity can be seen and analyzed as follows:

1. For the atmospheric tube furnace, the initial phase of Ni_2Si formed between 200-300°C with high contact resistivity values. With the temperature increase, transformation of the Ni_2Si phase to NiSi occurred, the lowest value of 6mohm/cm was obtained 2min annealing with a nitrogen atmosphere. The lowest contact resistivity at unexpectedly high furnace set temperature of 700°C is due to the amount of N_2 gas sent through the tube. Since the oxidation is tried to be eliminated at high temperatures, the nitrogen gas flow is increased so that the sample's actual temperature is lower than the set temperature of the tube furnace. The $NiSi_2$ phase is the third and last phase to transform, and until this phase, NiSi is stable and the dominant phase in forming the silicide layer. The contact resistivity value is increased, which is a sign that the 3rd phase became dominant as the temperature further increased. Those transformations do not occur at specific temperatures; however, the prevalent degrees at a temperature range are given in Figure 3.9.

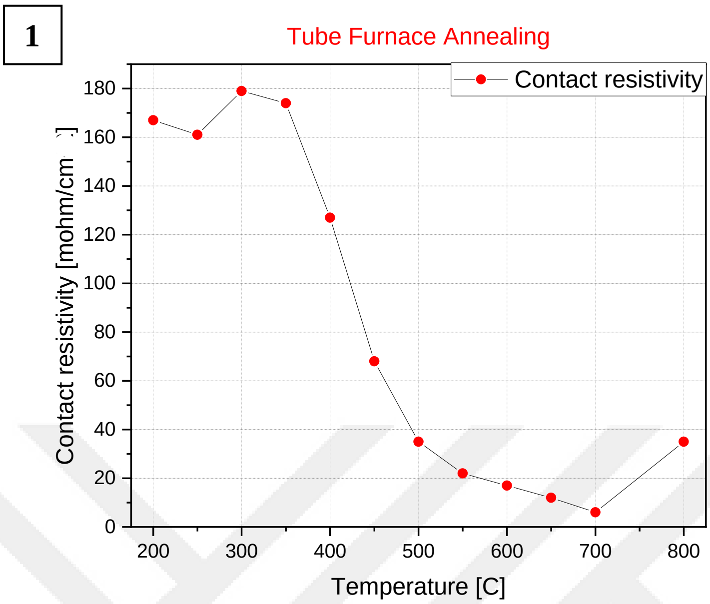

Figure 4.18: TLM contact resistivity results vs temperature (set value) annealed in tube furnace.

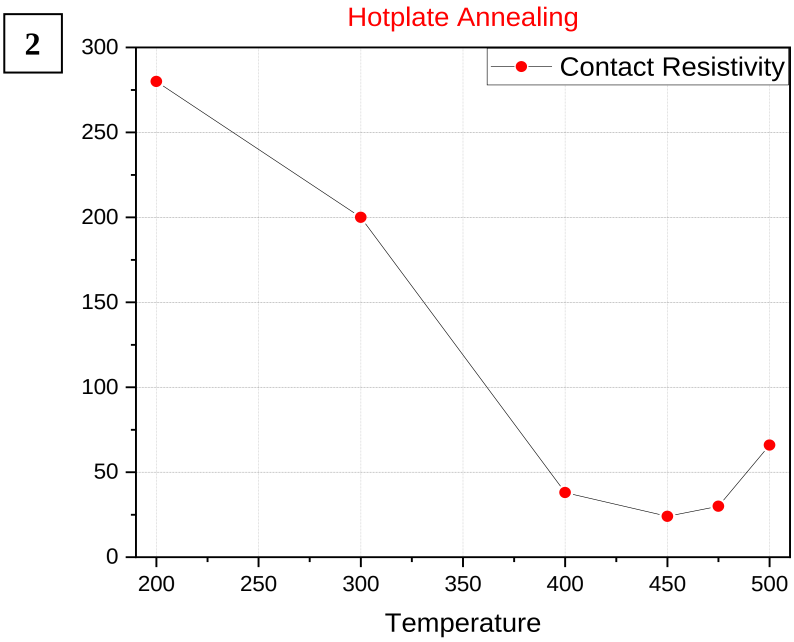

Figure 4.19 TLM contact resistivity results vs temperature annealed on hotplate.

2. The range is limited for the hot plate annealing due to the equipment and the maximum temperature obtained as 500°C. Due to the limitation of this temperature value, various time durations are applied in this method. Like the tube furnace annealing graph in Figure 4.13, Ni_2Si is formed between 200-300°C. After 300°C, the transformation from the first phase to the NiSi stable phase continued until the 550°C. However, the third $NiSi_2$ started to be replaced with more stable NiSi after 450°C, which explains the fluctuation of the contact resistivity. This results in the time variation in the 450°C to increase the NiSi phase formation percentage rather than increasing the temperature. Therefore, the lowest contact resistivity is obtained as 8mohm/cm^2 at 450°C with a 90-second duration of 3 times.

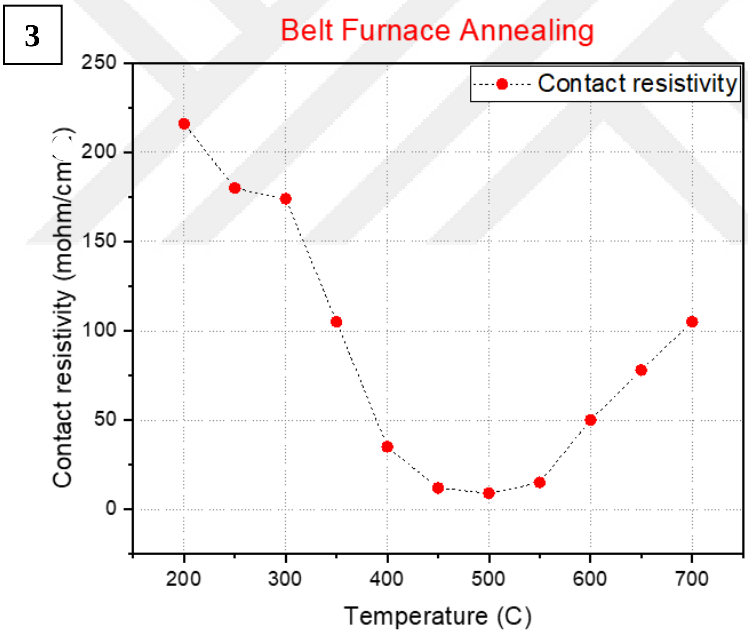

Figure 4.20 TLM contact resistivity results vs temperature annealed in belt furnace.

3. For belt furnace annealing, the nitrogen atmosphere is not presented. Samples annealed between 200-700°C with variable belt speeds. However, due to the oxidation during the belt process, the contact resistivity values are not obtained as

expected. The lowest contact resistivity result is around 15mohm/cm between 450-500°C with a belt speed of 400cmpm.

Consequently, the contact resistivity reduces from 400-200 mohm/cm² to 6 mohm/cm in a tube furnace setting, to 8 mohm/cm using a hotplate method, and to 10 mohm/cm in the belt furnace. The belt annealing technique also holds significance for its practicality in industry. However, during these experiments, the absence of sufficient N_2 gas within the belt environment, required for metal oxidation at high temperatures, is noted. Similar experiments could be conducted by incorporating the N_2 gas into the system, having the potential to even lower contact resistivity values.

Another aspect about annealing is shunting in p-n diodes as the temperature rises. By reducing the annealing temperature while extending the annealing time shunting probability can be decreased. However the main shunting comes from the laser ablation process. To clearly shown the laser impact on shunting, only silver is plated after the laser ablation. The shunt resistivity values of Ag plated and Ni/Cu/Ag metal stack are the same.

4.6 Cell Efficiency Results

For the 1BB cell design stripe, Ni/Cu/Ag-plated PERC cells were produced using 1064nm ns laser ablation, and Ni deposition was carried out with a current density of $2A/dm^2$ for 5 minutes. The front-plated Ni/Cu/Ag was subsequently annealed at 450°C for 270 seconds, and the resulting cells were characterized through I-V measurements.

The best results were achieved through hot plate annealing, yielding a fill factor (FF) of 69%, short-circuit current density (Jsc) of 36.2 mA/cm^2, open-circuit voltage (V_{OC}) of 631mV, and a contact resistivity of 6mohm/cm. It's worth noting that the I-V curve exhibits a shunting part, indicated by the bend in the y-axis. Significantly, this curvature is not attributed to Cu diffusion in the underlying layers but is a result of the laser ablation process. This is supported by the occurrence of the same shunting issue in silver plating. With further optimization, focusing on removing the dielectric layer, it is anticipated that this shunting can be eliminated, leading to even higher efficiency values.

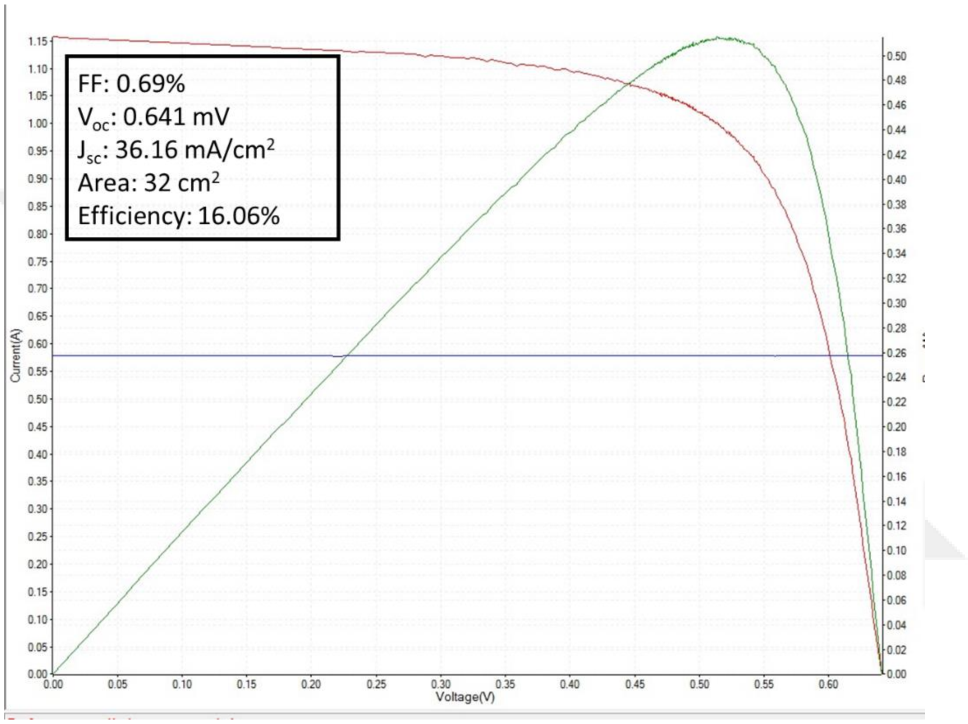

Figure 4.21 I-V curve result for plated Ni/Cu/Ag front metallization of PERC sample.

CHAPTER 5

CONCLUSION

To replace the expensive dominant screen printed Ag method with an alternative metal deposition technique, plating of Ni/Cu/Ag metal stack is a promising candidate with its comparative and less costly properties. Ni/Cu/Ag, metal stack plating, must overcome some challenges, such as having relatively lower adhesion. Before plating, a dielectric layer is opened with laser ablation, a precise and fast method. Lasers for the ablation selected already exist in the PV fabrication line such as 1064nm ns laser and 532nm ps lasers with optimum power, frequency, and scan speed parameters. The selected 1064nm laser gave less damage to the underlying junction without shunting, and these experiments were performed with a 1064nm laser due to adjustable scan speed or overlapping of spots. 1064nm ns laser ablation is completed, and the contact areas are opened for Ni seed layer deposition by light induced-bias assisted plating technique. The deposition parameters are selected as 2A/dm^2 externally, given the current density for the 5-minute duration. To ensure accurate TLM results, a complete stack of Ni/Cu/Ag is deposited as the contact. This stack is used for both TLM measurements and checking Cu diffusion. Additionally, a Cu conductive layer and an Ag capping layer are deposited to achieve an increased contact height. After the metal stack deposition, the samples are annealed in three different heat treatment tools: tube furnace, hot plate, and belt furnace with variable temperatures and durations. The formation of the Ni-Si interface with NiSi phases is investigated, and the lowest resistive phase of Ni_1Si_1 is obtained. The best result is obtained from the hot plate annealing as the contact resistivity of samples is around 7 mohm/cm at 450°C in 270 seconds. Therefore, a plated Ni/Cu/Ag metal stack for the front side metallization of PERC-type solar cells is formed with an optimized Ni seed layer, resulting in an FF of 69%.

In conclusion, the successful implementation of a Ni/Cu/Ag-plated front-side metal stack for PERC-type solar cells, accompanied by an optimized Ni seed layer deposition through less complex and industrially feasible fabrication methods, represents a promising alternative metallization technique. With suggested process flow, it is possible to reach compariable cell performance if the laser induced damages are eliminated by using more appropiate laser for being promising candidate to industrial production.

REFERENCES

[1] G. M. Wilson *et al.*, “The 2020 photovoltaic technologies roadmap,” *Journal of Physics D: Applied Physics*, vol. 53, no. 49. IOP Publishing Ltd, Dec. 02, 2020. doi: 10.1088/1361-6463/ab9c6a.

[2] B. Hallam *et al.*, “The silver learning curve for photovoltaics and projected silver demand for net-zero emissions by 2050,” *Progress in Photovoltaics: Research and Applications*, 2022, doi: 10.1002/pip.3661.

[3] J. Geissbuhler *et al.*, “Silicon heterojunction solar cells with copper-plated grid electrodes: Status and comparison with silver thick-film techniques,” *IEEE J Photovolt*, vol. 4, no. 4, pp. 1055–1062, 2014, doi: 10.1109/JPHOTOV.2014.2321663.

[4] L. Tous *et al.*, “Large area copper plated silicon solar cell exceeding 19.5% efficiency,” in *Energy Procedia*, Elsevier Ltd, 2011, pp. 58–65. doi: 10.1016/j.egypro.2012.05.008.

[5] A. Lennon, Y. Yao, and S. Wenham, “Evolution of metal plating for silicon solar cell metallisation,” *Progress in Photovoltaics: Research and Applications*, vol. 21, no. 7, pp. 1454–1468, Nov. 2013, doi: 10.1002/pip.2221.

[6] D. Chapin and C. Fuller, “The Silicon Solar Cell Turns 50.”

[7] “Photovoltaic Equipment International Technology Roadmap for Photovoltaic (ITRPV) 2022 Results,” 2023.

[8] C.-H. Lin, S.-P. Hsu, and W.-C. Hsu, “Silicon Solar Cells: Structural Properties of Ag-Contacts/Si-Substrate.” [Online]. Available: www.intechopen.com

[9] F. C. Krebs, J. Fyenbo, and M. Jørgensen, "Product integration of compact roll-to-roll processed polymer solar cell modules: Methods and manufacture using flexographic printing, slot-die coating and rotary screen printing," *J Mater Chem*, vol. 20, no. 41, pp. 8994–9001, Oct. 2010, doi: 10.1039/c0jm01178a.

[10] M. Hösel, R. R. Søndergaard, D. Angmo, and F. C. Krebs, "Comparison of fast roll-to-roll flexographic, inkjet, flatbed, and rotary screen printing of metal back electrodes for polymer solar cells," *Adv Eng Mater*, vol. 15, no. 10, pp. 995–1001, Oct. 2013, doi: 10.1002/adem.201300011.

[11] J. S. Lönnroth, V. Parail, D. C. McDonald, S. Saarelma, E. De La Luna, and M. Beurskens, "Dependence of pedestal performance on the characteristics of the H-mode pedestal," *Nuclear Fusion*, vol. 51, no. 1, Jan. 2011, doi: 10.1088/0029-5515/51/1/013003.

[12] M. and G. A. I. The International Association of Research Organizations for the Information, "Journal of Print and Media Technology Research," *The International Association of Research Organizations for the Information, Media and Graphic Arts Industries*, vol. 4, Mar. 2015.

[13] "United States Patent Office," 1966.

[14] Alberto Piqué and Pere Serra, "Laser Printing of Functional Materials," 2018.

[15] V. Arya *et al.*, "IMPROVEMENT OF SOLAR CELL EFFICIENCIES FOR ULTRASHORT-PULSE LASER CONTACT OPENING WITH NI-CU PLATED CONTACTS BY OPTIMIZED LCO-FFO PROCESSING ORDER."

[16] A. Dabirian *et al.*, "Metallization of Si heterojunction solar cells by nanosecond laser ablation and Ni-Cu plating," *Solar Energy Materials*

and Solar Cells, vol. 159, pp. 243–250, Jan. 2017, doi: 10.1016/j.solmat.2016.09.021.

[17] G. Poulain *et al.*, “Laser ablation mechanism of silicon nitride layers in a nanosecond UV regime,” in *Energy Procedia*, Elsevier Ltd, 2012, pp. 516–521. doi: 10.1016/j.egypro.2012.07.103.

[18] A. Dabirian *et al.*, “Metallization of Si heterojunction solar cells by nanosecond laser ablation and Ni-Cu plating,” *Solar Energy Materials and Solar Cells*, vol. 159, pp. 243–250, Jan. 2017, doi: 10.1016/j.solmat.2016.09.021.

[19] S. Rapp, G. Heinrich, M. Wollgarten, H. P. Huber, and M. Schmidt, “Physical mechanisms of SiNx layer structuring with ultrafast lasers by direct and confined laser ablation,” *J Appl Phys*, vol. 117, no. 10, Mar. 2015, doi: 10.1063/1.4914457.

[20] A. Knorz, M. Peters, A. Grohe, C. Harmel, and R. Preu, “Selective laser ablation of SiNx layers on textured surfaces for low temperature front side metallizations,” *Progress in Photovoltaics: Research and Applications*, vol. 17, no. 2, pp. 127–136, Mar. 2009, doi: 10.1002/pip.856.

[21] G. Heinrich, M. Wollgarten, M. Bähr, and A. Lawerenz, “Ultra-short pulsed laser ablation of silicon nitride layers: Investigation near threshold fluence,” in *Applied Surface Science*, Elsevier B.V., Aug. 2013, pp. 265–267. doi: 10.1016/j.apsusc.2012.10.122.

[22] A. Grohe *et al.*, “Progress in selective laser ablation of dielectric layers SELECTIVE LASER ABLATION OF DIELECTRIC LAYERS.” [Online]. Available: https://www.researchgate.net/publication/43607158

[23] M. Schulz-Ruhtenberg, D. Trusheim, J. Das, S. Krantz, and J. Wieduwilt, “Influence of pulse duration in picosecond laser ablation

of silicon nitride layers," in *Energy Procedia*, Elsevier Ltd, 2011, pp. 614–619. doi: 10.1016/j.egypro.2011.06.191.

[24] Y. C. Chang, S. Wang, R. Deng, S. Li, J. Ji, and C. M. Chong, "Investigation of laser doping and plating process for cost-effective PV metallization," *Solar Energy Materials and Solar Cells*, vol. 235, Jan. 2022, doi: 10.1016/j.solmat.2021.111445.

[25] X. Wang *et al.*, "Untangling the Mysteries of Plated Metal Finger Adhesion: Understanding the Contributions from Plating Rate, Chemistry, Grid Geometry, and Sintering," *IEEE J Photovolt*, vol. 6, no. 5, pp. 1167–1174, Sep. 2016, doi: 10.1109/JPHOTOV.2016.2589364.

[26] M. C. Raval *et al.*, "Study of Nickel Silicide Formation and Associated Fill-Factor Loss Analysis for Silicon Solar Cells with Plated Ni-Cu Based Metallization," *IEEE J Photovolt*, vol. 5, no. 6, pp. 1554–1562, Aug. 2015, doi: 10.1109/JPHOTOV.2015.2463741.

[27] A. Büchler *et al.*, "Interface oxides in femtosecond laser structured plated Ni-Cu-Ag contacts for silicon solar cells," *Solar Energy Materials and Solar Cells*, vol. 166, pp. 197–203, Jul. 2017, doi: 10.1016/j.solmat.2017.03.016.

[28] S. Rapp, G. Heinrich, M. Wollgarten, H. P. Huber, and M. Schmidt, "Physical mechanisms of SiNx layer structuring with ultrafast lasers by direct and confined laser ablation," *J Appl Phys*, vol. 117, no. 10, Mar. 2015, doi: 10.1063/1.4914457.

[29] G. Heinrich, M. Bähr, K. Stolberg, T. Wütherich, M. Leonhardt, and A. Lawerenz, "Investigation of ablation mechanisms for selective laser ablation of silicon nitride layers," in *Energy Procedia*, Elsevier Ltd, 2011, pp. 592–597. doi: 10.1016/j.egypro.2011.06.188.

[30] “Operating manual Laser System ILS TT R&D laser system for solar cell processing.” [Online]. Available: www.innolas-solutions.com

[31] S. Furukawa and an Mehregany, “Electroless plating of nickel on silicon for fabrication of high-aspect-ratio microstructures,” 1996.

[32] A. Büchler *et al.*, “Localization and characterization of annealing-induced shunts in Ni-plated monocrystalline silicon solar cells,” *Physica Status Solidi - Rapid Research Letters*, vol. 8, no. 5, pp. 385–389, 2014, doi: 10.1002/pssr.201409036.

[33] A. Büchler *et al.*, “Optimizing Adhesion of Laser Structured Plated Ni-Cu Contacts with Insights from Micro Characterization,” in *Energy Procedia*, Elsevier Ltd, Aug. 2016, pp. 913–918. doi: 10.1016/j.egypro.2016.07.101.

[34] D. Connétable and O. Thomas, “First-principles study of nickel-silicides ordered phases,” *J Alloys Compd*, vol. 509, no. 6, pp. 2639–2644, Feb. 2011, doi: 10.1016/j.jallcom.2010.10.118.

[35] S. H. Lee, A. U. Rehman, S. H. Lee, and E. G. Shin, “Improved adhesion of Ni/Cu/Ag plated contacts with thermally formed nickel silicon interface for C-SI solar cells,” *Mater Lett*, vol. 161, pp. 181–184, Dec. 2015, doi: 10.1016/j.matlet.2015.08.063.

[36] A. Noya and M. B. Takeyama, “Low-Temperature Formation of NiSi2 Phase in Ni/Si System,” *Electronics and Communications in Japan*, vol. 99, no. 9, pp. 85–91, Sep. 2016, doi: 10.1002/ecj.11860.

[37] P. R. Ortega *et al.*, “Low-cost high-sensitive Suns-V oc measurement instrument to characterize c-Si solar cells.”

[38] S. Kluska *et al.*, “Electrical and Mechanical Properties of Plated Ni/Cu Contacts for Si Solar Cells,” in *Energy Procedia*, Elsevier Ltd, 2015, pp. 733–743. doi: 10.1016/j.egypro.2015.07.104.

[39] S. Zhu, R. L. Van Meirhaeghe, S. Forment, G. Ru, and B. Li, “Effects of the annealing temperature on Ni silicide/n-Si(1 0 0) Schottky contacts,” *Solid State Electron*, vol. 48, no. 1, pp. 29–35, Jan. 2004, doi: 10.1016/S0038-1101(03)00286-7.

[40] A. Grohe *et al.*, “Progress in selective laser ablation of dielectric layers SELECTIVE LASER ABLATION OF DIELECTRIC LAYERS.” [Online]. Available: https://www.researchgate.net/publication/43607158